ARTICLE IN PRESS

Nature Communications

https://doi.org/10.1038/s41467-026-70764-x

Article in Press

Ceramide disrupts TM9SF2-PGK1 axis to redirect PD-L1 trafficking and enhance antitumor immunity

Received: 1 June 2025

Accepted: 4 March 2026

Cite this article as: Zheng, Y., Yang, F., Wang, M. *et al.* Ceramide disrupts TM9SF2-PGK1 axis to redirect PD-L1 trafficking and enhance antitumor immunity. *Nat Commun* (2026). https://doi.org/10.1038/s41467-026-70764-x

Yi Zheng, Fan Yang, Mengmeng Wang, Zhiying Wang, Xindan Zhang, Chenxin Huo, Yapeng Zhang, Aiqing Nie, Wenshuo Lyu, Anran Dong, Man Li, Zhiyong Du, Shenghao Zhou, Luning Song, Wenpeng Jiang, Bowen Gu, Wei Zhao & Ting Dong

We are providing an unedited version of this manuscript to give early access to its findings. Before final publication, the manuscript will undergo further editing. Please note there may be errors present which affect the content, and all legal disclaimers apply.

If this paper is publishing under a Transparent Peer Review model then Peer Review reports will publish with the final article.

ARTICLE IN PRESS

© The Author(s) 2026. **Open Access** This article is licensed under a Creative Commons Attribution-NonCommercial-NoDerivatives 4.0 International License, which permits any non-commercial use, sharing, distribution and reproduction in any medium or format, as long as you give appropriate credit to the original author(s) and the source, provide a link to the Creative Commons licence, and indicate if you modified the licensed material. You do not have permission under this licence to share adapted material derived from this article or parts of it. The images or other third party material in this article are included in the article's Creative Commons licence, unless indicated otherwise in a credit line to the material. If material is not included in the article's Creative Commons licence and your intended use is not permitted by statutory regulation or exceeds the permitted use, you will need to obtain permission directly from the copyright holder. To view a copy of this licence, visit http://creativecommons.org/licenses/by-nc-nd/4.0/.

ARTICLE IN PRESS

Ceramide Disrupts TM9SF2-PGK1 Axis to Redirect PD-L1 Trafficking and Enhance Antitumor Immunity

Authors: Yi Zheng[1,2,3]†, Fan Yang[3]†, Mengmeng Wang[4]†, Zhiying Wang[3], Xindan Zhang[5], Chenxin Huo[3], Yapeng Zhang[3], Aiqing Nie[3], Wenshuo Lyu[3], Anran Dong[3], Man Li[1], Zhiyong Du[3], Shenghao Zhou[3], Luning Song[3], Wenpeng Jiang[6], Bowen Gu[7,8], Wei Zhao[2,3]*, Ting Dong[1]*

Affiliations:

[1]Department of Biochemistry, Institute of Medicinal Biotechnology, Chinese Academy of Medical Sciences and Peking Union Medical College, Beijing 100050, China

[2]Clinical Trials Center, Qilu Hospital, Cheeloo College of Medicine, Shandong University, Jinan 250012, China

[3]Department of Clinical Pharmacy, Institute of Clinical Pharmacology, Key Laboratory of Chemical Biology (Ministry of Education),State Key Laboratory of Discovery and Utilization of Functional Components in Traditional Chinese Medicine, School of Pharmaceutical Sciences, Cheeloo College of Medicine, Shandong University, Jinan 250012, China

[4]Department of Natural Product Chemistry, Key Laboratory of Chemical Biology the Ministry of Education, School of Pharmaceutical Sciences, Shandong University, Jinan 250012, China

[5]State Key Laboratory of Bioactive Substance and Function of Natural Medicines, Institute of Materia Medica, Chinese Academy of Medical Sciences and Peking Union Medical College, Xicheng District, Beijing 100050, China

[6]Thoracic Department of Shandong Provincial Hospital affiliated to Shandong First Medical University. No.324, Jingwu Road, Jinan 250012, China

[7]Program in Cellular and Molecular Medicine, Boston Children's Hospital, Boston, MA, USA

[8]Department of Pediatrics, Harvard Medical School, Boston, MA, USA

*Corresponding author. Email: Ting Dong, tingdong2025@pumc.edu.cn; Wei Zhao, zhao4wei2@hotmail.com

†These authors contributed equally to this work.

Abstract: The programmed cell death protein 1 (PD-1) / programmed death-ligand 1 (PD-L1) axis represents a cornerstone of cancer immunotherapy, yet the dynamic shuttling of PD-L1 between endosomal recycling and lysosomal degradation routes limits durable responses. Using a CRISPR screen targeting glycosphingolipid metabolism, we identify transmembrane 9 superfamily member 2 (TM9SF2) as a key regulator of PD-L1 levels. TM9SF2 orchestrates a dual mechanism: it recruits phosphoglycerate kinase 1 (PGK1) to promote PD-L1 recycling to the plasma membrane while dismantling the huntingtin-interacting protein 1-related protein (HIP1R)-mediated lysosomal degradation pathway. Genetic or pharmacological disruption of the TM9SF2-PGK1 complex depletes PD-L1 levels and boosts antitumor immunity. Further, the endogenous ceramide species Cer(d18:1/26:0) destabilizes this complex, triggering PD-L1 lysosomal destruction and potentiating antitumor immunity. These findings delineate a ceramide-gated sorting mechanism within the endosomal network, revealing a druggable metabolic switch to disrupt immune evasion and amplify checkpoint blockade efficacy.

INTRODUCTION

ARTICLE IN PRESS

Immunotherapy using immune checkpoint inhibitors has recently led to significant advancements in cancer treatment [1-3]. Immune checkpoint inhibitors, especially anti-programmed death-1 (PD-1)/PD-1 ligand 1 (PD-L1) agents, have demonstrated promising efficacy and broad applicability across various cancers [4,5]. However, not all cancer patients experience substantial benefits from these therapies, and the overall response rates remain relatively low for most cancer types [6]. Furthermore, the immune checkpoint inhibitor resistance poses a significant challenge to the clinical success of cancer immunotherapy [7-10].

The intracellular fate of PD-L1 is governed by two competing trafficking pathways: being degraded and eliminated in lysosomes, or accumulating in recycling endosomes and repopulating to the cell membrane [11,12]. The disruption of this homeostatic balance often through enhanced recycling or suppressed degradation results in pathological PD-L1 accumulation on tumor cells. This aberrant PD-L1 expression subsequently attenuates T cell effector functions and drives clinical resistance to immunotherapy. Therefore, elucidating the molecular machinery governing PD-L1 intracellular trafficking has become an urgent priority in the field, establishing this process as a crucial regulatory node for improving immune checkpoint blockade (ICB) efficacy [13-15].

Endocytic trafficking of PD-L1—including its sorting into recycling, degradative, or retrograde pathways—is essential for maintaining its balanced distribution and supporting anti-cancer immunity [12,13,16-20]. Several key regulators of PD-L1 recycling and degradation have been identified to date, including our most recent work on VPS11/18 [21]. However, the mechanisms governing its sorting between the degradative and recycling pathways remain unclear. Sphingolipids, major components of eukaryotic membranes, play critical roles in maintaining membrane integrity, endocytosis, protein sorting, and secretion [22,23] They are unevenly distributed within cellular organelles, particularly enriched in the trans-Golgi-PM-endosome axis [24], suggesting a potential link to endosomal transport. As an active sphingolipid, whether ceramide is essential for the selective sorting of internalized PD-L1 to the endosomal membrane or for its lysosomal degradation remains to be determined.

In this study, we identify the TM9SF2-PGK1 complex as a critical hub that governs the intracellular trafficking and recycling of PD-L1. Through a CRISPR screen targeting glycosphingolipid metabolism, TM9SF2 emerged as a key regulator of PD-L1 abundance. Mechanistically, TM9SF2 orchestrates a dual program to control PD-L1 fate: it recruits PGK1 to facilitate PD-L1 recycling to the plasma membrane, while simultaneously dismantling the HIP1R-mediated lysosomal degradation pathway. Disruption of the TM9SF2-PGK1 complex by the endogenous ceramide species Cer(d18:1/26:0) redirects internalized PD-L1 toward lysosomal degradation, thereby potentiating antitumor immunity. This intracellular regulatory axis presents a promising therapeutic strategy to overcome resistance and improve the efficacy of immune checkpoint blockade (ICB) therapy.

RESULTS

TM9SF family members stabilize PD-L1 and suppress CD8$^+$ T cell cytotoxicity

Sphingolipids, critical structural and signaling components of cellular membranes, regulate immune responses through their metabolic intermediates [25,26]. To investigate whether sphingolipid synthesis/metabolic pathway mediate PD-L1 expression, we conducted a CRISPR-Cas9 knockout (KO) screen targeting 50 genes involved in the sphingolipid synthesis/metabolic pathway with H460 non-small cell lung cancer (NSCLC) cells (Fig. 1A). After lentiviral transduction and puromycin selection, we isolated the lowest 10% of PD-L1-expressing cells (PD-L1^{low}) by fluorescence-activated cell sorting (FACS) at two time points (day-7 and day-15), followed by next-generation sequencing to quantify sgRNA abundance. Notably, sgRNAs targeting members of the transmembrane 9 superfamily (*TM9SF1-*

ARTICLE IN PRESS

4) exhibited significant enrichment in the PD-L1^{Low} populations compared to control cells (Fig. 1B and Fig. S1A), indicating that these genes are essential for maintaining PD-L1 expression in H460 cells.

In mammals, four members of transmembrane 9 superfamily (TM9SF1-4) have been identified [27-29], but the functions of the TM9SF family in PD-L1 regulation are poorly understood. We generated *TM9SF1-4* KO H460 cells using two distinct sgRNAs each. Ablation of all four TM9SF genes resulted in a decrease in total PD-L1 protein levels and cell surface expression (Fig. 1C and Fig. S1B-C). Conversely, overexpression of *TM9SF1-4* upregulated both total and cell surface PD-L1 levels (Fig. 1D and Fig. S1D). Notably, PD-L1 mRNA levels were not affected by *TM9SF1-4* knockout (Fig. S1E). To determine whether TM9SF1-4 influences PD-L1 protein stability, H460 cells were treated with cycloheximide (CHX) which inhibits protein synthesis. An accelerated PD-L1 degradation were observed upon *TM9SF1-4* ablation, suggesting that TM9SF1-4 can stabilize PD-L1 at the protein level (Fig. 1E and Fig. S1F).

To determine whether TM9SF2 suppresses tumor immunogenicity, we first established an *in vitro* co-culture system using primary human T cells and either WT or *TM9SF2* KO H460 cells (Fig. 1F and Fig. S1G). Genetic ablation of *TM9SF2* significantly enhanced T cell-mediated tumor cell killing, as indicated by reduced viability (Fig. 1G and Fig. S1H) and increased apoptosis (Fig. S1I-J) in *TM9SF2* KO cells. Furthermore, *TM9SF2*-deficient cells induced strong CD8$^+$ T cell activation, reflected by elevated IFN-γ production and surface CD107a expression (Fig. 1H-I and Fig. S1K-L). Notably, PD-L1 overexpression in *TM9SF2*-KO cells reversed the T cell–mediated growth inhibition (Fig. S1M-N), identifying TM9SF2 as a novel regulator of PD-L1–dependent immune evasion.

TM9SF2 promotes PD-L1-mediated immunosuppression in CD8$^+$ T cell

To test *in vivo* anti-tumor efficacy of TM9SFs, we established *Tm9sf1-4*-knockdown (KD) models in B16 melanoma and C1498 leukemia cells using shRNA silencing. These immunocompetent murine models provide superior capability for investigating CD8$^+$ T cell-mediated immunity in C57BL/6J hosts. Following subcutaneous implantation in C57BL/6J mice, *Tm9sf1-4* knockdown consistently suppressed tumor growth in both models (Fig. 2A-C and Fig. S2A-F). Moreover, *Tm9sf1-4* KD tumors demonstrated reduced PD-L1 surface levels on cancer and increased infiltration of CD8$^+$ T cells in the tumor microenvironment (TME) (Fig. 2D and Fig. S2G-M). Of note, CD8$^+$ T-cell depletion with an anti-CD8 antibody abrogated the tumor suppression by *Tm9sf2* KD (Fig. 2C and Fig. S2D-F), suggesting that the tumor suppression is mediated by CD8$^+$ T cell. CD8$^+$ T cells isolated from *Tm9sf1-4* KD tumors displayed elevated cytotoxicity, as indicated by elevated IFN-γ as well as externalized CD107a [30,31] (Fig. 2E-F and Fig. S2N-O). Furthermore, these cells displayed a less exhausted phenotype, consistent with the marked downregulation of the exhaustion markers PD-1 and Tim-3 (Fig. S2P).

We then generated *Tm9sf2* overexpression (OE) B16 or C1498 cells and the subcutaneously inoculated *Tm9sf2* OE tumors showed increased PD-L1 expression (Fig. 2G and Fig. S2Q-R) and tumor grew more rapidly than the control group (Fig. 2H and Fig. S2S). Meanwhile, tumor-infiltrating CD8$^+$ T cells exhibits decreased amounts of IFN-γ and CD107a, and displayed elevated levels of PD-1 and Tim-3 (Fig. 2I-K and Fig. S2T-V). Strikingly, administration with anti-PD-L1 completely reversed *Tm9sf2*-OE-driven tumor progression in B16 models (Fig. 2H-K, Fig. S2S and Fig. S2V). Thus, TM9SF2 promote tumor progression by stabilizing PD-L1 and suppressing CD8$^+$ T cell cytotoxicity.

TM9SF2 interacts with PGK1 to suppress CD8$^+$ T cell function

To understand how TM9SF2 regulates PD-L1, we conducted immunoprecipitation coupled with mass spectrometry (IP-MS) analysis with FLAG-tagged TM9SF2 in HEK293T cells. Among the high-confidence interactors identified, phosphoglycerate kinase 1 (PGK1) ranked as the top hit, suggesting it might play a role in TM9SF2-mediated PD-L1 regulation (Fig. 3A).

ARTICLE IN PRESS

PGK1 is a classic glycolytic enzyme that drives tumor progression via ATP synthesis, post-transcriptional regulation, and metabolic reprogramming [32,33]. However, its role in PD-L1 immune regulation remain unclear. We validated the interaction between TM9SF2 and PGK1 with Co-IP, and this interaction was further potentiated by IFN-γ stimulation (Fig. 3B). Knocking out *PGK1* markedly diminished both total cellular and surface PD-L1 levels, whereas *PGK1* overexpression resulted in an increased PD-L1 expression (Fig. 3C and Fig. S3A-C). Given PGK1's canonical role as a glycolytic enzyme, we next evaluated whether the TM9SF2-PGK1 complex regulates PD-L1 via glycolytic activity. Inhibiting glycolysis with 2-deoxy-D-glucose (2-DG) was not able to downregulate PD-L1 as observed in *PGK1* KO cells (Fig. S3D), suggesting that PGK1 regulates PD-L1 in a manner independent of its glycolytic function. *TM9SF2/PGK1* double KO (DKO) exhibited no additive reduction in PD-L1 levels compared to the single KOs (Fig. S3E), indicating their functional redundancy in regulating PD-L1.

Previous study showed that the phosphorylation at serine 203 (S203) modulates PGK1's subcellular trafficking [34], we generated the phosphorylation-deficient (S203A) and phosphomimetic (S203D) PGK1 mutants using site-directed mutagenesis. PGK1 S203D mutant enhanced TM9SF2 binding capacity and elevated PD-L1 expression, whereas the S203A mutant disrupted this interaction and diminished PD-L1 levels (Fig. 3D-E). We found that PGK1 stabilize PD-L1 through post-translational regulation, as *PGK1* KO accelerated PD-L1 protein degradation (Fig. 3F-G and Fig. S3F) without affecting its mRNA abundance (Fig. S3G).

To investigate the pro-tumorigenic functions of PGK1 *in vivo*, we generated *Pgk1* KD B16 and C1498 cells and evaluated their effects on tumor growth in C57BL/6J mice. *Pgk1* KD significantly suppressed tumor growth (Fig. 3H and Fig. S3H). Correspondingly, *Pgk1* KD tumors exhibited reduced PD-L1 total protein and surface levels and enhanced $CD8^+$ T cell infiltration in the TME (Fig. 3I and Fig. S3H-L). Tumor-infiltrating $CD8^+$ T cells in *Pgk1* KD tumors display enhanced effector functions, including higher secretion of IFN-γ and expression of CD107a (Fig. 3J and Fig. S3M), along with reduced levels of the exhaustion markers PD-1 and Tim-3 (Fig. S3N).

DC-PGKI was previously reported to be a potent PGK1 inhibitor [35]. Inhibiting PGK1 with DC-PGKI recapitulated *Pgk1* knockout phenotypes of reducing intracellular PD-L1 level, suppressing tumor growth, and augmenting T cell-mediated immunity *in vivo* (Fig. 3K-N and Fig. S3O-U). Conversely, *Pgk1* overexpression accelerated tumor growth and impaired $CD8^+$ T cell functionality, underscoring its role in negatively regulating PD-L1-dependent antitumor immunity (Fig. 3O-Q and Fig. S3V-Z). These findings position PGK1 as a potential target for ICB therapy.

TM9SF2-PGK1 maintains PD-L1 expression by facilitating endosomal recycling

To determine the mechanistic basis of TM9SF2-PGK1-mediated PD-L1 regulation, we performed quantitative proteomics following *TM9SF2* depletion. Selective dysregulation of endosomal recycling components was enriched in *TM9SF2* KD cells, notably the COMMD/CCDC22/CCDC93 (CCC) complexes, which play a critical role in recycling events [36] (Fig. 4A).

Disrupting PD-L1 endosomal trafficking reduces its membrane anchoring and enhances anti-tumor immunity [12,13]. We therefore investigated whether the PGK1-TM9SF2 axis operates through a similar mechanism. Using a PD-L1-APC antibody to tract the internalization and recycling of surface PD-L1 [12], we found that knockout of *PGK1* or *TM9SF2* significantly decreased surface PD-L1 levels due to defective endosomal recycling (Fig. 4B-D). Confocal microscopy revealed markedly diminished co-localization of PD-L1 with the recycling endosome marker RAB11 in *TM9SF2* or *PGK1* KO cells (Fig. 4E). Co-immunoprecipitation of HA-tagged PGK1 confirmed its interaction with TM9SF2 and RAB11 within endosomes, and this binding was enhanced following IFN-γ stimulation (Fig. 4F).

ARTICLE IN PRESS

We have confirmed that the phosphorylation of PGK1 at serine 203 is necessary for the interaction between TM9SF2 and PGK1. To investigate whether this post-translational modification regulates PGK1 trafficking, we examined the temporal phosphorylation dynamics following IFN-γ stimulation. Subcellular fractionation into endosomal membrane and cytosolic compartments revealed that S203-phosphorylated PGK1 is selectively enriched in endosomal membranes. This compartment-specific redistribution mirrors the spatial pattern previously observed under EGF stimulation [34], suggesting a conserved mechanism for phosphorylation-dependent membrane localization (Fig. S4A). Strikingly, the phosphomimetic S203D mutant displayed increased interaction with PD-L1 and TM9SF2 in endosomes, whereas the non-phosphorylatable S203A mutant showed the opposite trend (Fig. 4G). These findings indicate that phosphorylation of PGK1 at the S203 site is essential for PD-L1 endosomal recycling, a process regulated by the TM9SF2-PGK1 interaction.

Endocytosed proteins undergo sorting through endosomal pathways for either lysosomal degradation or plasma membrane recycling. To determine whether the TM9SF2-PGK1 axis promotes PD-L1 recycling while preventing lysosomal degradation, we performed live-cell imaging to track PD-L1 spatiotemporal dynamics. Genetic ablation of either *TM9SF2* or *PGK1* redirected PD-L1 trafficking from recycling to degradative pathways, as evidenced by two complementary findings: reduced PD-L1 surface expression (Fig. S4B) and enhanced lysosomal accumulation quantified through increased co-localization with LAMP1 (Fig. S4C). Given that ubiquitination is a critical signal for the lysosomal degradation of PD-L1 [18], we performed immunoprecipitation of PD-L1 in *TM9SF2* or *PGK1* KO and WT cells, and found that the loss of neither TM9SF2 nor PGK1 altered PD-L1 ubiquitination levels (Fig. S4D-E). Thus, TM9SF2-PGK1 maintains the endocytosed PD-L1 by endosomal recycling instead of lysosomal degradation.

TM9SF2-PGK1 complex hinders lysosomal sorting by degrading the PD-L1 lysosomal carrier HIP1R

To investigate how the TM9SF2-PGK1 axis allows PD-L1 to evade lysosomal trafficking, we conducted quantitative proteomic profiling in *PGK1* KO cells. Significant upregulation of lysosomal sorting machinery components, particularly HIP1R—a key adaptor protein responsible for directing PD-L1 to lysosomes—was observed upon *PGK1* depletion [19] (Fig. 5A). And the elevated HIP1R protein levels were confirmed in *PGK1* and *TM9SF2* KO cells with Western blot (Fig. 5B-C and Fig. S5A-B), while *HIP1R* mRNA expression remained unchanged (Fig. S5C).

To understand how HIP1R is regulated by PGK1, we performed the CHX chase assay and found that *PGK1* deficiency significantly extended HIP1R protein half-life, whereas *PGK1* overexpression accelerated its degradation (Fig. 5D and Fig. S5D). Ectopic HA-PGK1 expression enhanced HIP1R polyubiquitination, which was further amplified under IFN-γ stimulation (Fig. 5E). Importantly, phosphorylation of PGK1 at S203 was crucial for its regulation of HIP1R ubiquitin-dependent degradation, S203A mutation abolished the PGK1-HIP1R interaction and diminished HIP1R ubiquitination (Fig. 5F and Fig. S5E).

PGK1 has been reported to recognize the dileucine-based sorting signal that directs endosomal EGFR to the lysosome [34]. Notably, HIP1R (966–979) possesses a similar dileucine motif [19]. To further examine whether PGK1 can recognize HIP1R through the dileucine motif, we constructed plasmids expressing both full-length HIP1R and a truncated version lacking residues HIP1R (966–979). Co-IP assays revealed that PGK1 specifically binds to the dileucine motif of HIP1R, as this interaction was abolished upon motif deletion (Fig. 5G). Furthermore, IFN-γ stimulation significantly enhanced PGK1-HIP1R binding (Fig. 5G), suggesting IFN-γ-induced phosphorylation of PGK1 may also participate in the interaction with HIP1R and its functional execution. To assess the functional relevance of this interaction, we overexpressed GFP-tagged constructs containing either the wild-type dileucine motif (GFP-S1) or a mutant version with leucine-to-alanine substitutions (GFP-S2) (Fig. 5H). Strikingly, *PGK1* deficiency

ARTICLE IN PRESS

markedly stabilized GFP-S1 but had no effect on GFP-S2 (Fig. 5I and Fig. S5F), indicating that PGK1 selectively targets the dileucine motif for degradation. These findings collectively demonstrate that PGK1 regulates HIP1R stability through direct recognition of its dileucine motif, mirroring its known role in EGFR trafficking.

Cer(d18:1/26:0) dissociates the TM9SF2-PGK1 complex to suppress PD-L1 expression and promote antitumor immunity

Given that PGK1 and TM9SF2 are both involved in sphingolipid metabolism [37,38], we hypothesized that specific sphingolipid intermediates might regulate TM9SF2-PGK1 complex assembly and downstream pathways. Targeted lipidomic profiling of *TM9SF2*-knockdown H460 cells versus wild-type controls identified 12 ceramide species with differential abundance (Fig. 6A). To interrogate this lipid-protein interplay, we treated H460 cells with commercially available ceramide standards (or their metabolically stable analogs) for 40 hours. Strikingly, Cer(d18:1/26:0) induced the most dramatic reduction in PD-L1 protein levels (Fig. 6B-C). Ceramides are synthesized by ceramide synthase enzymes (CERS), which exhibit distinct specificity for their acyl-CoA substrates [39]. We generated *CERS1-6* knockout H460 cell lines and evaluated PD-L1 levels (Fig. S6A). Depletion of *CERS3*, responsible for synthesizing Cer(d18:1/26:0), produced the most pronounced changes in PD-L1 levels, while overexpression of *CERS3* significantly downregulated PD-L1 levels (Fig. S6A-B). CHX chase assays showed that Cer(d18:1/26:0) treatment or *CERS3* overexpression reversed the PD-L1 stabilization and restored HIP1R degradation induced by *TM9SF2/PGK1* overexpression (Fig. 6D-E and Fig. S6C-G). Importantly, although TM9SF2 has been linked to ganglioside GM3 (Gb3) synthesis [37], we found that Gb3 does not contribute to TM9SF2-mediated PD-L1 regulation, underscoring the specificity of the ceramide-dependent pathway described here (Fig. S6H).

To investigate whether Cer(d18:1/26:0) disrupts the interaction between TM9SF2 and PGK1, thereby affecting PD-L1, we performed Co-IP and found that Cer(d18:1/26:0) treatment weakened the TM9SF2-PGK1 interaction (Fig. 6F). In addition, we analyzed the subcellular localization of PD-L1 using immunofluorescence labeling. Cer(d18:1/26:0) treatment reduced the colocalization of PD-L1 with recycling endosome markers (RAB11 and CD147) while increasing its association with the lysosomal marker LAMP1 (Fig. 6G and Fig. S6I-J). These findings suggest that Cer(d18:1/26:0) disrupts the PGK1-TM9SF2 interaction, thereby redirecting PD-L1 from recycling endosomes (RAB11/CD147) to lysosomes (LAMP1) and promoting its degradation.

We further examined the anti-tumor effects of Cer(d18:1/26:0) in B16 melanoma and C1498 acute myeloid leukemia (AML) models *in vivo* (Fig. 6H and Fig. S6K). Compared to the vehicle group, Cer(d18:1/26:0) treatment significantly inhibited tumor growth (Fig. 6I and Fig. S6L-M). Consistent with the reduced tumor burden, ex vivo analysis revealed lower PD-L1 levels on cancer cells and a higher percentage of $CD8^+$ T cells in the TME following Cer(d18:1/26:0) treatment (Fig. 6J and Fig. S6N-Q). Furthermore, tumor-infiltrating $CD8^+$ T cells exhibited increased effector functions, including enhanced IFN-γ secretion and CD107a expression, compared to those in untreated parental tumors (Fig. 6K and Fig. S6R).

Therapeutic potential for targeting TM9SF2-PGK1 complex in human lung cancer

Our findings suggest that the TM9SF2-PGK1 complex functions as a ceramide-responsive signaling hub, regulating PD-L1 sorting within the endosomal system and contributing to cancer immune evasion. To further investigate the clinical association between members of the TM9SF family and cancer prognosis, we compared their expression between normal cells and tumors in the Cancer Genome Atlas (TCGA) database. Bioinformatic analyses across multiple cancer types revealed that the *TM9SF1-4* gene signature is upregulated in lung adenocarcinoma (LUAD) and exhibits a negative correlation with overall survival

ARTICLE IN PRESS

in AML patients (Fig. 7A-B and Fig. S7A-B). Additionally, PGK1 expression was upregulated while HIP1R was downregulated in LUAD (Fig. 7A and Fig. S7A). Immunofluorescent staining of LUAD tissue microarrays further demonstrated a positive correlation of TM9SF2 with PD-L1 expression levels (Fig. 7C and Fig. S7C). To evaluate the potential clinical therapeutic value of these findings, tumor cells were isolated from lung cancer patients and treated with DC-PGKI or Cer(d18:1/26:0) (Fig. 7D). Western blot and flow cytometry analyses revealed that treatment with DC-PGKI and Cer(d18:1/26:0) resulted in a significant reduction of PD-L1 and an increase in HIP1R levels (Fig. 7E-F and Fig. S7D). To verify whether the reduction of PD-L1 expression by the two aforementioned compounds occurs through the TM9SF2-PGK1 complex-mediated pathway, we labeled PD-L1 to monitor its intracellular trafficking from the plasma membrane to endosomal or lysosomal compartments. Following treatment with Cer(d18:1/26:0) or DC-PGKI, a reduction in PD-L1 colocalization with RAB11 and plasma membrane markers was observed, accompanied by an increase in colocalization with the lysosomal marker LAMP1 (Fig. 7G and Fig. S7E). Collectively, these results suggest therapeutic potential to enhance antitumor immune responses by targeting TM9SF2-PGK1 complex formation to modulate PD-L1 trafficking and recycling (Fig. 7H).

DISCUSSION

Immune checkpoint blockade targeting the PD-1/PD-L1 pathway has emerged as a potent cancer treatment strategy [1,2,4,5,7,8], though its efficacy is limited by diverse resistance mechanisms. A key contributor to this resistance is the antibody-induced internalization and recycling of PD-L1, which leads to a neutralization of antibody without blocking PD-L1. Preventing lysosomal degradation of PD-L1 is crucial for maintaining its recycling back to the cell membrane. PD-L1 expression in tumor cells is regulated at multiple levels. A plethora of studies have identified critical regulators of PD-L1 intracellular trafficking and lysosomal degradation, highlighting potential targets to improve immunotherapy efficacy [12,13,16-20]. However, whether a specific sorting mechanism directs PD-L1 toward endosomal recycling versus lysosomal degradation remains unexplored. Our study identifies the TM9SF2-PGK1-RAB11 axis as a critical regulator of PD-L1 intracellular trafficking, diverting it from lysosomal degradation to sustain surface expression.

TM9SF2, a conserved member of the transmembrane 9 superfamily, contains a large N-terminal extracellular domain and nine transmembrane regions [27,29,37]. It is primarily localized to early endosomes and the Golgi apparatus [28,40], and is involved in glycosphingolipid biosynthesis and frequently upregulated in cancer [41,42]. Phosphoglycerate kinase 1 (PGK1), a key glycolytic enzyme, catalyzes the conversion of 1,3-bisphosphoglycerate to 3-phosphoglycerate, producing the first ATP in glycolysis. PGK1 is highly expressed in various cancers. Post-translational modifications of PGK1, including phosphorylation and acetylation, were found to be responsible for its and subcellular translocation to mitochondria and the nucleus, thereby enhancing glycolytic activity and supporting cancer cell growth [43,44]. However, how this complex coordinate membrane protein trafficking remains poorly understood. Our study showed that TM9SF2 and PGK1 form a complex with RAB11 to orchestrate PD-L1 recycling (Fig. 4E-F). Disrupting this axis rerouted PD-L1 to LAMP1^{+} lysosomes (Fig. S4B-C), with PGK1 phosphorylation at S203 serving as a molecular switch: the S203D mutant enhanced recycling (Fig. 4G), while S203A promoted lysosomal degradation (Fig. 5F and S5E). These data position TM9SF2-PGK1 as spatial gatekeepers of PD-L1 trafficking, ensuring its plasma membrane retention.

Sphingolipids are essential membrane components involved in cellular, developmental, and signaling processes, particularly in endomembrane transport, Golgi-mediated protein sorting, cell polarity, intercellular communication, and plasma membrane signaling [45]. As a central building block and bioactive metabolite of sphingolipid family, ceramide is highly enriched in the plasma membrane. It is synthesized in the endoplasmic reticulum (ER) and transported to the *trans*-Golgi region, where it is converted into

ARTICLE IN PRESS

sphingomyelin [46]. As a potent tumor suppressor with pro-apoptotic properties, ceramide plays a critical role in cell death induced by several common chemotherapeutic agents [47,48].

Beyond its function as a second messenger, ceramide was reported to regulate the endosomal recycling of transport proteins [49] and facilitate the formation of membrane subdomains, aiding the sorting of specific proteins in pre- or post-Golgi compartments [50,51]. Our research uncovered a metabolic checkpoint wherein the sphingolipid Cer(d18:1/26:0) destabilizes PD-L1 by dissociating TM9SF2-PGK1 (Fig. 6B-D, 6F and S6C-F).

Our study found that inhibition of *TM9SF2* or *PGK1* suppressed tumor growth, enhanced $CD8^+$ T-cell infiltration, and exhibited synergistic effects with anti-PD-L1 treatment (Fig. 2A-K, 3H-N, S2A-P, S3H-U). Conversely, *TM9SF2* or *PGK1* overexpression accelerated immune evasion (Fig. 2G-K, S2Q-V, 3O-Q and S3V-Z). Clinical correlations further supported our findings: TM9SF2/PGK1 expression levels predicted poor prognosis in LUAD and AML patients (Fig. 7A–B and S7A-B) and are highly correlated with PD-L1 expression level (Fig. 7C and S7C).

Although our work provides a strong preclinical rationale for targeting TM9SF2-PGK1 axis for anti-PD-L1 ICB resistance, key questions remain: (1) What specifically distinguishes Cer(d18:1/26:0) from other structurally similar sphingolipids in its ability to disrupt the TM9SF2-PGK1 interaction? (2) How do upstream signals, such as TNFα-induced ceramide bursts, regulate the sorting of PD-L1? (3) Does the TM9SF2-PGK1 complex regulate other immune checkpoints, such as CTLA-4, or other oncoproteins? Future studies remain to map the TM9SF2-PGK1 interactome, and investigate how ceramide disrupts TM9SF2-PGK1 interaction.

Overall, our research identified a TM9SF2-PGK1-ceramide axis that regulates PD-L1 stability through endosomal recycling, thus linking sphingolipid metabolism to immune evasion, and offers a roadmap for next-generation therapies targeting the crosstalk between sphingolipids and PD-L1. We highlight the therapeutic potential of this pathway with methods such as genetic ablation, PGK1 inhibition (DC-PGKI), and ceramide supplementation, which provide a strategic framework for overcoming resistance to ICB. Pharmacological targeting of the TM9SF2-PGK1 complex, both as a standalone treatment and in conjunction with ICB, warrants further clinical investigation in tumors exhibiting high levels of TM9SF2 and PGK1.

Methods

Ethics statement

For mice: Eight-week-old C57BL/6J male mice were obtained from Beijing Vital River Laboratory Animal Technology Co., Ltd. (China). They were maintained in individually ventilated cages at the Shandong University Model Animal Research Center, with a standard 14:10-h light: dark cycle, ambient temperature of 23-25 °C, humidity levels of 40-70% and full access to water and facility chow, following the guidelines set forth by the Animal Care and Utilization Committee of Shandong University, China. All animal studies were conducted in accordance with protocols approved by the Ethics Committee of Shandong University (Approval No. SYXK (Lu) 20230003). According to the approved protocol, the maximum allowable size for any solid tumor is 20 mm in any single dimension. This study strictly adhered to these requirements. Mice were humanely euthanized via carbon dioxide inhalation.

For patient samples: All human lung cancer specimens analyzed in this study were collected from surgical resections performed at the Second Hospital of Shandong University. The use of these clinical samples was reviewed and approved by the Institutional Ethics Committee of the Second Hospital of Shandong University (Approval No. KYLL2025362), and all procedures were conducted in full compliance with the relevant ethical regulations.

ARTICLE IN PRESS

Cell culture and treatment

HEK293T cells (Procell Corporation, #CL-0005), B16-F10 cells (Procell Corporation, #CL-0319), H460 cells (Procell Corporation, #CL-0299), and mouse AML cells (C1498) (ATCC, #TIB-49) were incubated in Dulbecco's Modified Eagle's Medium (DMEM, containing 10% fetal bovine serum (FBS) as well as 1% penicillin-streptomycin) (37 °C, 5% CO_2). For IFN-γ treatment, cells were administered IFN-γ (100 ng/mL) for 48 hours unless indicated otherwise. All ceramide standards (or their metabolically stable analogs) were given at 31.25 μM for 40 hours unless indicated otherwise. The reagents used in this study are listed in Supplementary Dataset 1.

Plasmids

To produce the pLenti-CRISPRv2-sgRNA plasmids for sphingolipid metabolic pathway related CRISPR-Cas9 knockout screen and *PGK1* knockout, we allowed sgRNAs to cool naturally to room temperature after heating to 95 °C for 5 minutes in an annealing buffer. We cloned the annealed sgRNAs into a *Bsm*BI-digested pLenti-CRISPRv2 vector (#52961, Addgene, USA). The sgRNAs were designed using crispor.tefor.net. CRISPR sgRNA sequences for *TM9SF1-4*/*PGK1*/*CERS1-6* knockout are listed in Supplementary Dataset 2 and sgRNA sequences for sphingolipid metabolic pathway related CRISPR-Cas9 knockout screen are listed in Supplementary Dataset 3.

For the FLAG-tagged *TM9SF1-4*, *CERS3* and *CD274* plasmids, we purchased FLAG-tagged *TM9SF3* plasmid (#P56344) and FLAG-tagged *TM9SF4* plasmid (#P58124) from MIAOLING BIOLOGY. We inserted human *TM9SF1*, *CERS3* and *CD274* PCR products into pcDNA3.1-3×FLAG vector (#182494, Addgene, USA) and inserted *TM9SF2* products into the *Hind*III and *Eco*RI sites of pCMV-T7-MCS-3×FLAG-Neo vector (#P1303, MIAOLING BIOLOGY, China).

To generate constructs for HA-tagged *PGK1*, PCR fragments underwent digestion with *Eco*RI and *Xho*I before being inserted into the pcDNA3.1-HA vector (#128034, Addgene, USA). The pCDH-*Pgk1* plasmids were produced by inserting the synthesized cDNA coding mouse *Pgk1* into pCDH-CMV-MCS-EF1-mcherry-T2A-puro vector (#IGV-LV-a-003, Guangzhou IGE Biotechnology Co., Ltd., China) using *Eco*RI/*BamH*I MCS.

For the construction of plasmids encoding PGK1 variants, including phosphorylation mutants (S203A and S203D) and PAM locus mutants, pcDNA3.1-HA-*PGK1*$^{p.Ser203Ala}$ and pcDNA3.1-HA-*PGK1*$^{p.Ser203Asp}$ were developed using a Mut Express II Fast Mutagenesis Kit V2 (#C214-01, Vazyme, China), with pcDNA3.1-HA-*PGK1* serving as the template. These constructs were subsequently employed as templates to generate the pcDNA3.1-HA-*PGK1*$^{p.Ser203Ala,\ c.978G>A}$ and pcDNA3.1-HA-*PGK1*$^{p.Ser203Asp,\ c.978G>A}$ plasmids, designed to block PAM detection by mutating the NGG site to a sequence compatible with specificity-modified Cas9.

The MYC-tagged *HIP1R* construct was generated by inserting the PCR product into the pcDNA3.1-MYC vector (#176045, Addgene, USA). For the GFP-tagged *HIP1R* construct, the fragments were inserted into the *Xba*I-*Eco*RI region of pCDH-CMV-MCS-EF1-Blast-EGFP.

The GFP-S1 plasmid was acquired from Tsingke Biotechnology Co., Ltd. by cloning cDNA with an HA-tag and the designated peptide (S1) into pEGFP-C1 via the *Bgl* II/*EcoR* I multiple cloning sites. To generate the leucine-to-alanine mutant, GFP-S2 was developed using a Mut Express II Fast Mutagenesis Kit V2, with GFP-S1 as a template. Similarly, the GFP-tagged *HIP1R*$^{\Delta 966\text{-}979}$ mutant was generated with *HIP1R*-GFP as a template.

We amplified the *TM9SF2*, *PGK1*, *HIP1R*, and *CD274* genes from A549 cDNA, *Pgk1* from L929 cDNA, *TM9SF1* from the pCMV-SPORT6-*TM9SF1* plasmid (#P4018, MIAOLING BIOLOGY, China), and *CERS3* from the pCDNA3.1-HA-*CERS3* plasmid (#P2224, MIAOLING BIOLOGY, China). All primers

ARTICLE IN PRESS

were procured from Sangon Biotech, and plasmid sequences were confirmed through DNA sequencing. Primer sequences are listed in Supplementary Dataset 4.

Hairpin shRNAs targeting the coding sequences of mouse *Tm9sf1-4* and *Pgk1*, transcripts were also generated by Tsingke Biotechnology Co., Ltd. and inserted into the pLKO.1-mCherry-Puro vector. Short hairpin sequences are provided in Supplementary Dataset 5.

Stable cell line generation

To generate *TM9SF1-4* or *PGK1* knockout (KO) clones, CRISPR-Cas9 technology was employed as previously described [52]. pLenti-CRISPRv2-sgRNA plasmids were introduced into HEK293T cells grown in 6-well plates via polyethylenimine (PEI) transfection, along with packaging plasmids PMD2.G and PSPAX at a ratio of 0.25:0.15:0.20 to produce lentivirus. Viral extracts were harvested at 24 h and 48 h after transfection and applied to H460 cells supplemented with polybrene (10 μg/mL). Puromycin selection (2 μg/mL) was subsequently performed for several days to isolate transduced cells.

For generating *TM9SF2*/*PGK1* double-knockout (dKO) clones, *TM9SF2* KO H460 cells (3×10^4 cells/well) were plated in 12-well plates, and then they were transduced using lentiviral particles (pLenti-CRISPRv2-sgRNA *PGK1*) in the presence of polybrene to facilitate *PGK1* knockout. Single-cell clones were generated from polyclonal populations using limiting dilution and validated by immunoblotting to confirm the loss of TM9SF2 and PGK1 protein expression. For *Pgk1* overexpression (OE) in B16 and C1498 cells, pCDH-*Pgk1* plasmids, along with packaging plasmids, were transfected into HEK293T cells to produce lentiviruses. B16 and C1498 cells underwent infection with the produced lentiviruses with polybrene, and subsequently, puromycin selection was applied. *Tm9sf2* OE B16 and C1498 cells were generated using LV-*Tm9sf2* viral filtrate (#63315-22, GeneChem Co., Ltd.).

For knockdown (KD) of mouse *Tm9sf1-4* or *Pgk1*, lentiviral vectors expressing the respective shRNAs were transfected into HEK293T cells to produce control and knockdown lentiviruses. B16 and C1498 cells were infected twice with lentivirus-containing culture medium and polybrene at 37 °C for 24 and 48 hours. To maximize KD efficiency, infected cells underwent puromycin selection for several days and were characterized using confocal microscopy.

Puromycin-resistant KD, KO, or OE clones were extracted via single-cell dilution cloning from polyclonal groups and validated by immunoblotting for the respective proteins.

Mouse subcutaneous tumor-bearing model

For syngeneic melanoma or AML models, 1×10^6 B16 or C1498 cells modified with the indicated shRNAs or overexpression constructs were resuspended in 100 μL of saline and introduced subcutaneously into the flanks of C57BL/6J mice to produce tumors. On the day of inoculation with tumor cells, mice were administered with anti-CD8 monoclonal antibody (mAb), anti-PD-L1 mAb, DC-PGKI, or Cer(d18:1/26:0).

For checkpoint therapy, mice received intraperitoneal injections of 200 μg anti-CD8 mAb or 200 μg anti-PD-L1 mAb (or isotype control) on the 0, 3rd, 6th, 9th, and 12th day.

For PGK1 inhibitor treatment, mice received intraperitoneal injections of DC-PGKI which was formulated in a solution of 10% DMSO and 90% PBS at 10 and 5 mg/kg/day, respectively, or a control solution consisting of 10% DMSO in PBS (v/v), for one week.

For treatment with Cer(d18:1/26:0), C57BL/6J mice were injected intraperitoneally with vehicle or Cer(d18:1/26:0) (10 and 20 mg/kg/day) for one week. Cer(d18:1/26:0) was mixed in saline containing sodium carboxymethyl cellulose (0.5%) and Tween 80 (5%), whereas control animals received saline with the same additives.

ARTICLE IN PRESS

For C1498 tumors, tumor sizes were evaluated every three days. At the designated time after tumor cell inoculation, mice were euthanized and their tumors were collected for subsequent analysis.

Preparation of ceramide: cholPC

Our approach had slight modifications from a previous protocol [53]. Ceramides and cholPC were solubilized in pure chloroform at a concentration of 12.5 mM. ceramide and cholPC were combined at 1:1, dried with nitrogen, and rehydrated using PBS to attain a final concentration of 3.125 mM for each lipid (3.125 mM Cer:3.125 mM cholPC or cholPC: blank). Rehydrated lipids were sonicated for approximately 1 hour until fully dissolved (55 °C). Lipid mixtures were mixed with cell cultures at a 1:100 dilution, making a final level of 31.25 μM for each ceramide.

CRISPR screen

H460 cells were infected with a focused sgRNA library designed to target genes involved in phospholipid metabolism, with 4 sgRNAs per gene. At 48 hours post-infection, cells were enriched for transduced populations via selection with 2 μg/mL puromycin for 72 hours. PD-L1^{low} cells, low 10% of the population, were enriched via two fluorescence-activated cell sorting (FACS) rounds on days 7 and 15 following library transduction. For the first sort, at least 2×10^7 cells were obtained with trypsin, stained on ice for 15 minutes using an APC anti-human PD-L1 antibody, and washed with PBS. Cells exhibiting low PD-L1 expression were isolated using a BD Influx flow cytometer. Genomic DNA (gDNA) was isolated from sorted and unselected populations of mutagenized cells on day 15 by Genomic DNA Purification Kit (#B518251, Sangon Biotech, China) and sent to Novogene for sequencing.

Immunoblotting

Whole-cell or tissue lysates were prepared using RIPA buffer (Solarbio, China) with a 1% protease inhibitor cocktail and 1 mM PMSF. The samples were kept on ice for 10min before centrifuge (10,000 × *g*, 4 °C, 15 min). Tissue samples were pre-minced and ground in lysis buffer prior to extraction. Proteins were quantified using a bicinchoninic acid (BCA) assay kit (#BL1673A, Biosharp, China). Cell lysates were combined with 5× loading buffer containing 10% 2-mercaptoethanol and heated for 5min for denaturation at 100 °C, except for TM9SF1-4 detection, where samples were denatured at 4 °C for 30 minutes. Forty micrograms of protein per sample were isolated by 10% SDS-PAGE gel and transferred to a polyvinylidene fluoride (PVDF) membrane (Millipore). The membrane was incubated with blocking buffer (EpiZyme, Shanghai, China) for 1 hour at room temperature, then probed with the primary antibody overnight at 4 °C (for details, see Supplementary Dataset 1). Following three sequential 5-minute washes in TBST, the membranes were probed with HRP-associated secondary antibodies (goat anti-rabbit IgG or goat anti-mouse IgG) (1:10,000 dilution in TBST), with incubation proceeding for 60 min (room temperature). Bands were observed using an ECL western blot detection substrate (#32106, Thermo Fisher). For fluorescent detection, Goat anti-Rabbit IgG H&L (IRDye® 800CW) or Goat anti-Mouse IgG H&L (IRDye® 800CW) (1:10,000) were used, and membranes underwent scanning with an Odyssey CLx Imaging System (LI-COR Biosciences). Gray intensity quantification was performed using ImageJ (Fiji).

Immunoaffinity purification-mass spectrometry (IP-MS)

HEK293T cells were plated in triplicate 10 cm culture dishes and introduced alongside FLAG-tagged *TM9SF2* plasmid using PEI. Following a 48-hour incubation period, cellular material was collected and homogenized in lysis solution supplemented with 1% protease inhibitor cocktail and 1 mM PMSF. The lysate was subsequently subjected to centrifugation (13,000 × *g*, 15 minutes, 4 °C) to remove cellular debris. Clarified supernatants were mixed with 30 μL anti-FLAG beads (Sigma) for overnight conjugation at 4 °C. After extensive washing (3 ×) with chilled lysis buffer, the immobilized protein complexes were flash-frozen in liquid nitrogen and subjected to LC-MS/MS analysis.

ARTICLE IN PRESS

Coimmunoprecipitation and ubiquitination assays

To investigate protein-protein interactions, HEK293T or H460 cells were transiently transfected with specified plasmids through PEI-mediated transfection for 48h. After transfection, cells were harvested and subjected to immunoprecipitation with magnetic affinity beads conjugated to FLAG, HA, MYC, or GFP antibodies (Cell Signaling Technology) at 4 °C. Antibody-associated complexes were extensively washed (3 ×) with ice-cold lysis buffer, followed by incubation with loading buffer adding 10% β-mercaptoethanol, and 5 min boiling (100 °C) minutes prior to immunoblotting. For TM9SF2 detection, proteins were eluted from beads using 3 × FLAG or HA peptides and denatured without boiling. For Cer(d18:1/26:0) treatment, HEK293T cells expressing FLAG-tagged *TM9SF2* and HA-tagged *PGK1* were treated with 31.25 μM Cer(d18:1/26:0) for 40 hours, followed by coimmunoprecipitation analysis.

Ubiquitination assays were conducted on co-immunoprecipitation (Co-IP) lysates. Specifically, HEK293T or H460 cells were transfected with various plasmids, with or without stimulation by IFN-γ (100 ng/mL). MYC-tagged protein complexes were immobilized on MYC affinity beads and subsequently washed sequentially with chilled lysis buffer. Immunoblot analysis was performed using an anti-ubiquitin antibody to detect ubiquitinated proteins.

Immunofluorescence imaging

H460 cells, subjected to genetic or pharmacological disruption, including the depletion of PGK1 and TM9SF2 and treatment with ceramide, were utilized in this study. Additionally, cancer cells isolated from lung cancer patients were treated with either DC-PGKI or Cer(d18:1/26:0). All cell types subsequently underwent the following procedures:

The cells were fixed with 4% paraformaldehyde and permeabilized with 0.1% Triton X-100. Non-specific binding sites were blocked with 5% BSA for 1 hour. Cells were then incubated with primary antibodies in PBST (phosphate-buffered saline containing 0.01% Tween-80) under gentle agitation at 4 °C for 16 hours. Following three successive 5-minute rinses with PBST, samples were exposed to species-matched secondary antibodies in the dark for 1 hour at 25 °C. After rinsing, cells were counterstained with DAPI (1 μg/mL) for 10 minutes. Finally, fluorescence signals were captured using a confocal laser scanning microscope (Andor Dragonfly 200) at a resolution of 1024 × 1024 pixels with a 63 × oil immersion objective. Colocalization assessment was performed using ImageJ. Briefly, the red and green traces in the curves correspond to their respective fluorescence channels. Fluorescence intensity values were quantified using the Plot Profile tool in ImageJ along annotated white lines in merged immunofluorescence images, allowing assessment of how red and green fluorophore signal intensities vary with distance.

Characterization of PD-L1 on cell surfaces

H460 cells were trypsinized and rinsed twice using ice-cold PBS. Cells were stained using APC anti-human *CD274* antibody under gentle rotation at 4 °C for 60 min in light-protected conditions. Following two additional washes with chilled PBS, antibody-labeled cells were analyzed using flow cytometry.

RNA isolation and qRT-PCR analysis

Total RNA was isolated using a NcmSpin Cell/Tissue RNA Kit (#M5105, NCM Biotech, China). First-strand cDNA synthesis followed a SPARKscript IIRT SuperMix for qPCR (#AG0305-B, Sparkjade, China) following the manufacturer's directions. We performed RT-qPCR analysis on a qRT-PCR system using SYBR. Quantitative analysis was performed via comparative threshold cycle ($2^{-\Delta\Delta CT}$) method with data normalized to *GAPDH* housekeeping gene expression levels. The primer sequences for qRT-PCR were as follows:

human *CD274*: forward, 5'-TCACTACACAGCCCTCCTAA-3',

ARTICLE IN PRESS

reverse, 5'-ACACCAGAATATGGCCAAGAG-3';

human *HIP1R*: forward, 5'-AGATGCTGTGCGGAGGATTGAG-3',

reverse, 5'-TGCAGGCTAGTGGATGTCGTCA-3';

human *GAPDH*: forward, 5'-GAGTCCACTGGCGTCTTCAC-3',

reverse, 5'-TTCACACCCATGACGAACAT-3'.

T cell-mediated tumor cell lethality

T cells were negatively enriched from healthy donor peripheral blood mononuclear cells (PBMCs) employing an EasySep™ isolation system (#17951, STEMCELL Technologies) via negative selection. The isolated T cells were maintained in RPMI 1640 medium. Polyclonal activation was achieved via co-stimulation using ImmunoCult™ CD3/CD28/CD2 T Cell Activator (#10970, STEMCELL Technologies) and recombinant human IL-2 (1000 U/mL, #78036, STEMCELL Technologies) for 3 days. For cell apoptosis assays: sgNTC and sg*TM9SF2* H460 cells were plated using 1×10^5 cells/well in 12-well plates, and PBMC-derived effector T cells were included at an effector-to-target ratio of 2:1. After 48-hour co-incubation, cells were collected. After dual PBS washing cycles, cells were subjected to the Annexin V-FITC/7-AAD Apoptosis Detection Kit (#40311ES60, Yeasen, China) at 4 °C for 15 min in light-protected conditions to differentiate early from late apoptotic, as well as necrotic cells. Flow cytometry quantified apoptosis based on the proportion of Annexin V-positive and 7-AAD-positive cells. Anti-PD-L1 treatment served as a positive control. Data attainment was carried out with the BD FACSymphony™ A3 Cell Analyzer, and analysis was conducted with FlowJo software.

For crystal violet staining, sgNTC and sg*TM9SF2* H460 cells were co-cultured with T cells sorted from PBMCs (effector-to-target ratio of 2:1) for 48 hours. Residual living cancer cells were assessed using crystal violet staining.

For the CCK-8 assay, sgNTC and sg*TM9SF2* H460 cells were placed into 96-well plates with 100 μL culture medium per well, then co-cultured with activated T cells (1:2 ratio) for 48 hours. Residual cancer cells were characterized using CCK-8 staining. Specifically, 10 μL of CCK-8 solution was administered into each well and incubated for 2 hours at 37 °C/5% CO_2, after which absorbance at 450 nm, corresponding to formazan product formation, was determined.

T cells analysis was performed using flow cytometric techniques. Cell viability was assessed with Fixable Viability Dye. For surface marker evaluation, cells were washed and incubated with Brilliant Violet 421 anti-human CD8α and Brilliant Violet 785 anti-human CD107a.

Intracellular interferon gamma (IFN-γ) detection involved cell fixation/permeabilization with the True-Nuclear™ Transcription Factor Buffer Set (#424401, BioLegend, USA), followed by staining with PE-IFN-γ following the producer's protocol. Isolates were acquired on a BD LSR Fortessa Cell Analyzer (BD Biosciences). Data were analyzed using FlowJo v10 (Treestar Inc.) and GraphPad Prism 9.0.

Tissue microarray analysis

A paraffin-embedded LUAD tissue microarray was obtained from Bioaitech Co. (R076Lu01). All tissues were collected under strict ethical standards with complete donor informed consent. Immunofluorescence analysis of PD-L1 and TM9SF2 expression was performed as described above.

Tumor cell isolation

Single-cell suspensions were generated from lung cancer patient-derived tumor samples through rapid and gentle mechanical dissociation, enzymatic digestion using collagenase IV for 1 h at 37 °C, and

ARTICLE IN PRESS

subsequent filtration. Tumor cells were then isolated using a tumor cell isolation kit and grown in DMEM (containing 10% FBS and 1% penicillin-streptomycin).

Tumor inoculation and dissection

For tumor dissection, B16 or C1498 tumor tissues were dissected, imaged, and digested using Liberase TM (7.7 mg/mL) and DNase I (100 mg/mL). Tumor fragments were strained using 70-μm strainers (BD Biosciences) to generate single-cell isolates for flow cytometric analysis.

For tumor-infiltrating lymphocytes (TILs), single cell isolates were Fc receptor-blocked using TruStain FcX (1:100) for 15 min, and stained using: AF700-CD45.2 (1:200), PE-Cy7-CD3 (1:1000), BV786-CD8 (1:1000), PerCP-CD4 (1:300), BV421-IFN-γ (1:300), PE-CD107a (1:300), PE-TOX (1:100), PE-Tim-3 (1:200), BV605-PD-1 (1:300) and Fixable Viability Dye (1:1000). We first used Fixable Viability Dye to exclude dead cells in flow cytometry data. Data acquisition was performed on the BD FACSymphony™ A3 Cell Analyzer, and assessment was performed using FlowJo. The gating strategy is detailed in Supplementary Fig. 8.

For PD-L1 expression on tumor cells, single-cell isolates were Fc-blocked, stained using APC-PD-L1 (1:300), and analyzed using the same workflow.

Antibodies used in this study are listed in Supplementary Dataset 1.

Endocytosis and recycling assays

To evaluate PD-L1 recycling, a recycling assay was performed as previously outlined [54]. In short, sgNTC and sg*TM9SF2*/*PGK1* H460 cells were Fc-blocked (1:100 dilution) and labeled with a purified anti-human PD-L1 antibody (1:500 dilution) for 0.5 h at 4 °C. After labeling, cells were rinsed with chilled medium and incubated at 37 °C for 30 minutes to facilitate internalization of antibody-bound PD-L1. Surface-bound antibodies were removed using a low pH buffer (IMDM with 1× Pen/Strep and 50 mM sodium, pH 3.5), followed by two PBS washes and incubation in complete medium. Baseline internalized PD-L1 levels were measured immediately after washing (t_0), and the recycling pool was quantified after incubation at 37 °C for designated time points (t_x). Surface-recycled PD-L1 was detected using an APC-conjugated goat anti-mouse IgG secondary antibody (1:200). The total residual PD-L1 assembly was assessed after fixation and permeabilization, followed by incubation with the same secondary antibody for 45 minutes at room temperature. Cells were rinsed and assessed via flow cytometry.

PD-L1 recycling levels were determined by the ratio of recycled surface PD-L1 to the total residual pool. To study PD-L1 storage after internalization, H460 cells were detached with TrypLE Express, incubated on ice, and rinsed using RPMI medium (5% FCS, 30 mM HEPES). Surface PD-L1 was labeled using anti-PD-L1 antibody for one hour, washed twice, and resuspended in RPMI. A baseline sample (t_0) was collected. Cells were then incubated at 37 °C to allow PD-L1 internalization. At designated time points, samples were diluted in ice-cold PBS, washed, and stained using Alexa Fluor-647-conjugated anti-mouse secondary antibody over 0.5 h. After washing, samples were analyzed via flow cytometry.

$$\text{Surface PD-L1 at baseline } (t_0) = S(t_0) / A(t_0) \quad (1)$$

$$\text{Surface PD-L1 at a time point } (t_x) = S(t_x) / A(t_x) \quad (2)$$

$$\text{PD-L1 Recycling efficiency} = [S(t_x) / A(t_x)] - [S(t_0) / A(t_0)] \quad (3)$$

Subcellular fractionation

To separate cellular fractions, H460 cells, either treated or untreated with IFN-γ, were suspended in homogenization buffer consisting of 20 mM HEPES-KOH (pH 7.4), 250 mM sucrose, 1 mM EDTA, and protease inhibitors. Cell lysis was achieved by repeated passage through a 25-gauge needle, followed by

ARTICLE IN PRESS

centrifugation of the clarified lysates at 800 × g for 5 minutes to remove unbroken cells. The resulting supernatants were further centrifuged (13,000 × *g*, 10min) to isolate large membrane fractions. Remaining supernatants underwent velocity centrifugation at 100,000 × *g* for 1 hour, separating light membranes containing endosomal fractions from the cytosolic fraction. All fractions (1:1) were electrophoresed via SDS-PAGE and evaluated by Western blotting.

Lipidomics

Lipidomic profiling of sh*TM9SF2* and shNC H460 cells was conducted by PTM-biolab Co., Inc. Briefly, cell samples were thawed on ice and extracted using a solvent mixture containing internal standards. After centrifugation, the upper organic layer was collected, dried under vacuum, and reconstituted in a solution (ACN:IPA = 1:1, v/v). Metabolite analysis was performed using LC-ESI-MS/MS with an ExionLC AD coupled to a QTRAP® 6500+ mass spectrometer. Data were log2-transformed, mean-centered, and validated through a permutation test with 200 iterations.

Proteomics

For proteomic profiling, H460 cells with *TM9SF2* knockdown or *PGK1* knockout were collected and processed by Spectra Biotechnologies (Shanghai). Briefly, peptides were separated using an UltiMate 3000 LC system coupled to a timsTOF Pro 2 mass spectrometer, with elution over a 60-minute gradient on a C18 column at a flow rate of 400 nL/min. Data-independent acquisition (DIA) was performed in diaPASEF mode using variable isolation windows and mobility-dependent collision energy. Raw data were processed in Spectronaut against a human UniProt database, with false discovery rate (FDR) filtering set at 1% and label-free quantification performed using MaxLFQ.

Statistical analysis

All data are presented as mean ± SD. Two-tailed student's t-test was used to compare all experimental groups against the control group. Significance levels were defined as *$p < 0.05$, **$p < 0.01$, ***$p < 0.001$, and ****$p < 0.0001$ in the figures. Statistical analyses were conducted using GraphPad Prism 10.1.2, and all experiments were independently repeated at least three times.

Data Availability

The lung adenocarcinoma data (TCGA-LUAD) used in this study are publicly available in the Database of Genotypes and Phenotypes (dbGaP) under accession number phs000178 (https://www.ncbi.nlm.nih.gov/projects/gap/cgi-bin/study.cgi?study_id=phs000178.v11.p8). The acute myeloid leukemia data (TARGET-AML) used in this study are publicly available in the dbGaP under accession number phs000218 (https://www.ncbi.nlm.nih.gov/projects/gap/cgi-bin/study.cgi?study_id=phs000218.v26.p8). The genomic and proteomic data generated in this study are publicly available as follows: The mass spectrometry proteomics data of sh*TM9SF2* and shNC H460 cells have been deposited to the ProteomeXchange Consortium via the PRIDE partner repository with the dataset identifier PXD061780 (https://www.ebi.ac.uk/pride/archive/projects/PXD061780). The raw data and search results of sgNTC and sg*PGK1* H460 cells have been uploaded to the iProX database under the accession number IPX0011331001 (https://www.iprox.cn//page/subproject.html?id=IPX0011331001). The raw data and search results of IP-MS analysis with FLAG-tagged TM9SF2 have been uploaded to the iProX database under the accession number IPX0015889001 (https://www.iprox.cn//page/subproject.html?id=IPX0015889001). The lipidomics data generated in this study have been deposited in the MetaboLights database under accession code MTBLS13838 (https://www.ebi.ac.uk/metabolights/MTBLS13838). The sequencing data from the focused CRISPR screen have been deposited to the NCBI GEO database under accession number GSE320531 (https://www.ncbi.nlm.nih.gov/geo/query/acc.cgi?acc=GSE320531). All additional data are available

ARTICLE IN PRESS

from the corresponding author (tingdong2025@pumc.edu.cn) upon request. Source data are provided with this paper.

References

1 Sanmamed, M. F. & Chen, L. A Paradigm Shift in Cancer Immunotherapy: From Enhancement to Normalization. *Cell* **175**, 313-326, doi:10.1016/j.cell.2018.09.035 (2018).

2 Kim, T. K., Vandsemb, E. N., Herbst, R. S. & Chen, L. Adaptive immune resistance at the tumour site: mechanisms and therapeutic opportunities. *Nature reviews. Drug discovery* **21**, 529-540, doi:10.1038/s41573-022-00493-5 (2022).

3 Kubli, S. P., Berger, T., Araujo, D. V., Siu, L. L. & Mak, T. W. Beyond immune checkpoint blockade: emerging immunological strategies. *Nature reviews. Drug discovery* **20**, 899-919, doi:10.1038/s41573-021-00155-y (2021).

4 Bonaventura, P. *et al.* Cold Tumors: A Therapeutic Challenge for Immunotherapy. *Frontiers in immunology* **10**, 168, doi:10.3389/fimmu.2019.00168 (2019).

5 Sharma, P., Hu-Lieskovan, S., Wargo, J. A. & Ribas, A. Primary, Adaptive, and Acquired Resistance to Cancer Immunotherapy. *Cell* **168**, 707-723, doi:10.1016/j.cell.2017.01.017 (2017).

6 Choi, S. H. *et al.* DRG2 is required for surface localization of PD-L1 and the efficacy of anti-PD-1 therapy. *Cell death discovery* **10**, 260, doi:10.1038/s41420-024-02027-x (2024).

7 Pang, K. *et al.* Research progress of therapeutic effects and drug resistance of immunotherapy based on PD-1/PD-L1 blockade. *Drug resistance updates : reviews and commentaries in antimicrobial and anticancer chemotherapy* **66**, 100907, doi:10.1016/j.drup.2022.100907 (2023).

8 Schoenfeld, A. J. & Hellmann, M. D. Acquired Resistance to Immune Checkpoint Inhibitors. *Cancer cell* **37**, 443-455, doi:10.1016/j.ccell.2020.03.017 (2020).

9 Ribas, A. & Wolchok, J. D. Cancer immunotherapy using checkpoint blockade. *Science (New York, N.Y.)* **359**, 1350-1355, doi:10.1126/science.aar4060 (2018).

10 Sharma, P. *et al.* Immune checkpoint therapy-current perspectives and future directions. *Cell* **186**, 1652-1669, doi:10.1016/j.cell.2023.03.006 (2023).

11 Li, C. W. *et al.* Eradication of Triple-Negative Breast Cancer Cells by Targeting Glycosylated PD-L1. *Cancer cell* **33**, 187-201.e110, doi:10.1016/j.ccell.2018.01.009 (2018).

12 Burr, M. L. *et al.* CMTM6 maintains the expression of PD-L1 and regulates anti-tumour immunity. *Nature* **549**, 101-105, doi:10.1038/nature23643 (2017).

13 Ren, Y. *et al.* TRAPPC4 regulates the intracellular trafficking of PD-L1 and antitumor immunity. *Nature communications* **12**, 5405, doi:10.1038/s41467-021-25662-9 (2021).

14 Yu, X. *et al.* PD-L1 translocation to the plasma membrane enables tumor immune evasion through MIB2 ubiquitination. *The Journal of clinical investigation* **133**, doi:10.1172/jci160456 (2023).

15 Yi, M., Niu, M., Xu, L., Luo, S. & Wu, K. Regulation of PD-L1 expression in the tumor microenvironment. *Journal of hematology & oncology* **14**, 10, doi:10.1186/s13045-020-01027-5 (2021).

16 Ye, Z. *et al.* Manipulation of PD-L1 Endosomal Trafficking Promotes Anticancer Immunity. *Advanced science (Weinheim, Baden-Wurttemberg, Germany)* **10**, e2206411, doi:10.1002/advs.202206411 (2023).

17 Guo, H. *et al.* Insights into the role of derailed endocytic trafficking pathway in cancer: From the perspective of cancer hallmarks. *Pharmacological research* **201**, 107084, doi:10.1016/j.phrs.2024.107084 (2024).

18 Lemma, E. Y., Letian, A., Altorki, N. K. & McGraw, T. E. Regulation of PD-L1 Trafficking from Synthesis to Degradation. *Cancer immunology research* **11**, 866-874, doi:10.1158/2326-6066.Cir-22-0953 (2023).

ARTICLE IN PRESS

19 Wang, H. *et al.* HIP1R targets PD-L1 to lysosomal degradation to alter T cell-mediated cytotoxicity. *Nature chemical biology* **15**, 42-50, doi:10.1038/s41589-018-0161-x (2019).

20 Xu, X. *et al.* Hsc70 promotes anti-tumor immunity by targeting PD-L1 for lysosomal degradation. *Nature communications* **15**, 4237, doi:10.1038/s41467-024-48597-3 (2024).

21 Dong, T. *et al.* Targeting VPS18 hampers retromer trafficking of PD-L1 and augments immunotherapy. *Science advances* **10**, eadp4917, doi:10.1126/sciadv.adp4917 (2024).

22 Contreras, F. X. *et al.* Molecular recognition of a single sphingolipid species by a protein's transmembrane domain. *Nature* **481**, 525-529, doi:10.1038/nature10742 (2012).

23 Breslow, D. K. & Weissman, J. S. Membranes in balance: mechanisms of sphingolipid homeostasis. *Molecular cell* **40**, 267-279, doi:10.1016/j.molcel.2010.10.005 (2010).

24 Bieberich, E. Sphingolipids and lipid rafts: Novel concepts and methods of analysis. *Chemistry and physics of lipids* **216**, 114-131, doi:10.1016/j.chemphyslip.2018.08.003 (2018).

25 Hannun, Y. A. & Obeid, L. M. Sphingolipids and their metabolism in physiology and disease. *Nature reviews. Molecular cell biology* **19**, 175-191, doi:10.1038/nrm.2017.107 (2018).

26 Lee, M., Lee, S. Y. & Bae, Y. S. Functional roles of sphingolipids in immunity and their implication in disease. *Experimental & molecular medicine* **55**, 1110-1130, doi:10.1038/s12276-023-01018-9 (2023).

27 Chluba-de Tapia, J., de Tapia, M., Jäggin, V. & Eberle, A. N. Cloning of a human multispanning membrane protein cDNA: evidence for a new protein family. *Gene* **197**, 195-204, doi:10.1016/s0378-1119(97)00263-1 (1997).

28 Schimmöller, F., Díaz, E., Mühlbauer, B. & Pfeffer, S. R. Characterization of a 76 kDa endosomal, multispanning membrane protein that is highly conserved throughout evolution. *Gene* **216**, 311-318, doi:10.1016/s0378-1119(98)00349-7 (1998).

29 Lozupone, F. *et al.* The human homologue of Dictyostelium discoideum phg1A is expressed by human metastatic melanoma cells. *EMBO reports* **10**, 1348-1354, doi:10.1038/embor.2009.236 (2009).

30 Hoekstra, M. E. *et al.* Distinct spatiotemporal dynamics of CD8(+) T cell-derived cytokines in the tumor microenvironment. *Cancer cell* **42**, 157-167.e159, doi:10.1016/j.ccell.2023.12.010 (2024).

31 Aktas, E., Kucuksezer, U. C., Bilgic, S., Erten, G. & Deniz, G. Relationship between CD107a expression and cytotoxic activity. *Cellular immunology* **254**, 149-154, doi:10.1016/j.cellimm.2008.08.007 (2009).

32 Qiu, A. *et al.* Phosphoglycerate Kinase 1: An Effective Therapeutic Target in Cancer. *Frontiers in bioscience (Landmark edition)* **29**, 92, doi:10.31083/j.fbl2903092 (2024).

33 Liu, H. *et al.* PRMT1-mediated PGK1 arginine methylation promotes colorectal cancer glycolysis and tumorigenesis. *Cell death & disease* **15**, 170, doi:10.1038/s41419-024-06544-6 (2024).

34 Chu, S. L. *et al.* Phosphoglycerate kinase 1 acts as a cargo adaptor to promote EGFR transport to the lysosome. *Nature communications* **15**, 1021, doi:10.1038/s41467-024-45443-4 (2024).

35 Liao, L. *et al.* A potent PGK1 antagonist reveals PGK1 regulates the production of IL-1β and IL-6. *Acta pharmaceutica Sinica. B* **12**, 4180-4192, doi:10.1016/j.apsb.2022.05.012 (2022).

36 Singla, A. *et al.* Endosomal PI(3)P regulation by the COMMD/CCDC22/CCDC93 (CCC) complex controls membrane protein recycling. *Nature communications* **10**, 4271, doi:10.1038/s41467-019-12221-6 (2019).

37 Yamaji, T. *et al.* A CRISPR Screen Identifies LAPTM4A and TM9SF Proteins as Glycolipid-Regulating Factors. *iScience* **11**, 409-424, doi:10.1016/j.isci.2018.12.039 (2019).

38 He, Y. *et al.* PGK1-mediated cancer progression and drug resistance. *American journal of cancer research* **9**, 2280-2302 (2019).

39 Alizadeh, J. *et al.* Ceramides and ceramide synthases in cancer: Focus on apoptosis and autophagy. *European journal of cell biology* **102**, 151337, doi:10.1016/j.ejcb.2023.151337 (2023).

ARTICLE IN PRESS

40 Tanaka, A. *et al.* Genome-Wide Screening Uncovers the Significance of N-Sulfation of Heparan Sulfate as a Host Cell Factor for Chikungunya Virus Infection. *Journal of virology* **91**, doi:10.1128/jvi.00432-17 (2017).

41 Li, Q. *et al.* LINC01232 exerts oncogenic activities in pancreatic adenocarcinoma via regulation of TM9SF2. *Cell death & disease* **10**, 698, doi:10.1038/s41419-019-1896-3 (2019).

42 Clark, C. R. *et al.* Transposon mutagenesis screen in mice identifies TM9SF2 as a novel colorectal cancer oncogene. *Scientific reports* **8**, 15327, doi:10.1038/s41598-018-33527-3 (2018).

43 Fu, Q. & Yu, Z. Phosphoglycerate kinase 1 (PGK1) in cancer: A promising target for diagnosis and therapy. *Life sciences* **256**, 117863, doi:10.1016/j.lfs.2020.117863 (2020).

44 Nie, H. *et al.* O-GlcNAcylation of PGK1 coordinates glycolysis and TCA cycle to promote tumor growth. *Nature communications* **11**, 36, doi:10.1038/s41467-019-13601-8 (2020).

45 Fougère, L., Mongrand, S. & Boutté, Y. The function of sphingolipids in membrane trafficking and cell signaling in plants, in comparison with yeast and animal cells. *Biochimica et biophysica acta. Molecular and cell biology of lipids* **1869**, 159463, doi:10.1016/j.bbalip.2024.159463 (2024).

46 Hanada, K., Kumagai, K., Tomishige, N. & Kawano, M. CERT and intracellular trafficking of ceramide. *Biochimica et biophysica acta* **1771**, 644-653, doi:10.1016/j.bbalip.2007.01.009 (2007).

47 Morad, S. A. & Cabot, M. C. Ceramide-orchestrated signalling in cancer cells. *Nat Rev Cancer* **13**, 51-65, doi:10.1038/nrc3398 (2013).

48 Ogretmen, B. & Hannun, Y. A. Biologically active sphingolipids in cancer pathogenesis and treatment. *Nat Rev Cancer* **4**, 604-616, doi:10.1038/nrc1411 (2004).

49 Finicle, B. T. *et al.* Sphingolipids inhibit endosomal recycling of nutrient transporters by inactivating ARF6. *Journal of cell science* **131**, doi:10.1242/jcs.213314 (2018).

50 Hanada, K. *et al.* Molecular machinery for non-vesicular trafficking of ceramide. *Nature* **426**, 803-809, doi:10.1038/nature02188 (2003).

51 Turpin-Nolan, S. M. & Brüning, J. C. The role of ceramides in metabolic disorders: when size and localization matters. *Nature reviews. Endocrinology* **16**, 224-233, doi:10.1038/s41574-020-0320-5 (2020).

52 Cong, L. & Zhang, F. Genome engineering using CRISPR-Cas9 system. *Methods in molecular biology (Clifton, N.J.)* **1239**, 197-217, doi:10.1007/978-1-4939-1862-1_10 (2015).

53 York, A. G. *et al.* IL-10 constrains sphingolipid metabolism to limit inflammation. *Nature* **627**, 628-635, doi:10.1038/s41586-024-07098-5 (2024).

54 Chen, X. *et al.* A membrane-associated MHC-I inhibitory axis for cancer immune evasion. *Cell* **186**, 3903-3920.e3921, doi:10.1016/j.cell.2023.07.016 (2023).

Acknowledgments

This work was supported by the National Key R&D Project on Biomedical Frontiers (2025YFC3409705) to T.D., Beijing Nova Program (2025-20250484836) to T.D., Shandong Provincial Natural Science Foundation of China (ZR2024MB138) to T.D., National Natural Science Foundation of China (82474005 to Y.Z., 82373957 to W.Z.), Central Public-interest Scientific Institution Basal Research Fund (2025-RC350-01, 2025-JKCS-28) to T.D., National Key R&D Program of China (2023YFC2706100) to W.Z. and Y.Z., Taishan Scholar Program of Shandong Province (tstp20230660) to W.Z..

Author contributions

Conceptualization: T.D.; bioinformatics, data analyses and visualization: F.Y. and M.W.; AML syngeneic mouse models: F.Y., Y.Z., C.H. and A.N.; solid tumor syngeneic mouse models: F.Y., M.W. and C.H.; tumor dissection: W.L., A.D., Z.D., S.Z., and L.S.; mechanistic studies: F.Y. and M.W.; clinical sample collection: W.J.; project administration: D.T., W.Z. and Y.Z.; data curation: T.D., M.W., Z.W., X.Z. and

M.L.; funding acquisition: T.D., W.Z. and Y.Z.; writing—original draft: T.D. and M.W.; Writing—review & editing: T.D., M.W., F.Y., B.G., Z.W., X.Z. and Y.Z.. All authors reviewed the results and approved the final version of the manuscript.

Competing interests

Authors declare that they have no competing interests.

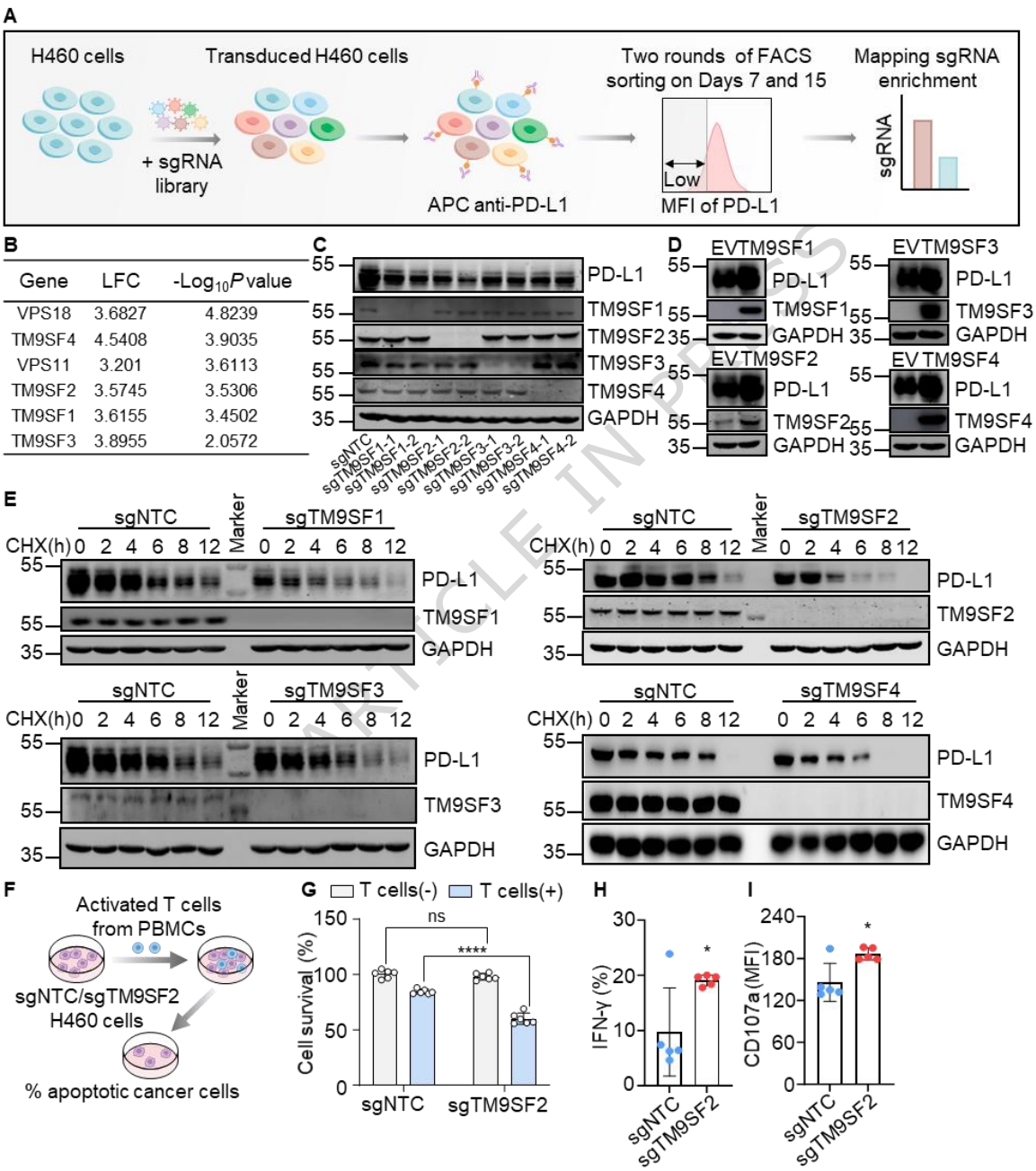

Fig. 1. TM9SF family members stabilize PD-L1 and suppress CD8⁺ T cell cytotoxicity.
(A) An outline of the CRISPR-Cas9-based deletion library screen targeting genes related to sphingolipid synthesis or transport essential for cell surface PD-L1 expression. H460 cells expressing Cas9 were mutagenized with a focused lentiviral sgRNA library and PD-L1^{low} cells enriched by FACS sorting.
(B) Significant hits identified from cellular screens are shown. LFC: The log2 fold change of sgRNA.

(C) PD-L1 expression in sgNTC and sgTM9SF1-4 H460 cells was analyzed by Western blot. NTC: No Template Control.
(D) Western blot assessment to evaluate PD-L1 expression in H460 cells overexpressing FLAG-tagged TM9SF1-4 versus empty vector (EV). FLAG antibody is used for the detection of TM9SF1/3/4. TM9SF2 antibody is used for the detection of TM9SF2.
(E) The lifetime of PD-L1 was assessed in sgNTC and sgTM9SF1-4 H460 cells administered cycloheximide (CHX, 25 μg/mL) over time. PD-L1 levels were standardized to GAPDH.
(F) A schematic overview of the T-cell-reliant cytotoxicity is shown. H460 cells transduced using TM9SF2-targeting sgRNA or control sgRNA were co-cultured with activated T cells. Cytotoxicity was evaluated through clonogenic assays, survival analyses, and apoptosis measurements.
(G) Cell viability showing T-cell cytotoxicity in H460 cells with TM9SF2 depletion following activated T cells co-culture.
(H-I) Quantitative analysis of IFN-γ and CD107a expression in $CD8^+$ T cells derived from co-culture are shown (n = 5 independent experiments).
Data are presented as mean ± SD. *p < 0.05; **p < 0.01; ***p < 0.001; ****p < 0.0001. Source data are provided as a Source Data file.

ARTICLE IN PRESS

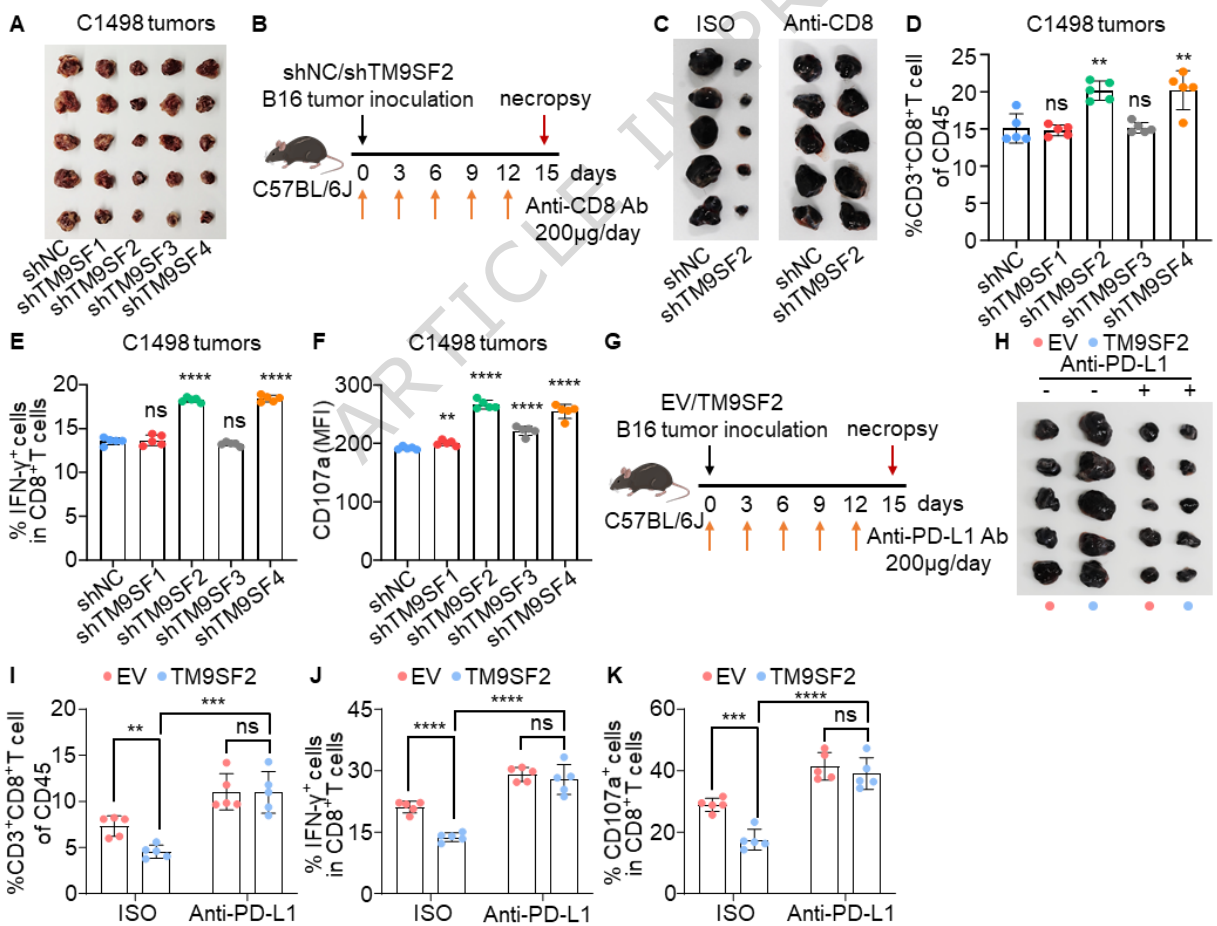

Fig. 2. TM9SF2 promotes PD-L1-mediated immunosuppression in $CD8^+$ T cell.
For **A** and **D-F**, a mouse tumor model using C57BL/6J mice transplanted with C1498 cells transduced with shRNA targeting TM9SFs or control.
(A) Representative images of control and TM9SFs-knockdown C1498 tumors.

ARTICLE IN PRESS

(B) Schematic of experimental procedures: For **C**, C57BL/6J mice subcutaneously injected with B16 cells transduced with TM9SF2-targeting shRNA or control, with or without CD8-depleting antibody treatment (200 μg on days 0, 3, 6, 9, and 12).
(C) Representative images of B16 tumors isolated from immunocompetent mice and $CD8^+$ T cell-depleted mice. ISO: Isotype Control.
(D) Proportions of tumor-permeating $CD8^+$ T cells in control and TM9SFs-knockdown C1498 tumors (n = 5 mice).
(E-F) Flow cytometry analysis of IFN-γ and CD107a level in control and TM9SFs-knockdown C1498 tumors (n = 5 mice).
(G) Schematic of experimental procedures: For **H-K**, C57BL/6J mice subcutaneously injected with B16 cells overexpressing TM9SF2 or EV control, with or without anti-PD-L1 antibody treatment (200 μg on days 0, 3, 6, 9, and 12).
(H) Representative images of B16 tumors isolated from mice with or without anti-PD-L1 antibody treatment.
(I) Proportions of tumor-permeating $CD8^+$ T cells in B16 tumors isolated from mice with or without anti-PD-L1 antibody treatment (n = 5 mice).
(J-K) Flow cytometry analysis of IFN-γ and CD107a levels in tumor-permeating $CD8^+$ T cells in B16 tumors isolated from mice with or without anti-PD-L1 antibody treatment (n = 5 mice).
Data are presented as mean ± SD. *p < 0.05; **p < 0.01; ***p < 0.001; ****p < 0.0001. Source data are provided as a Source Data file.

ARTICLE IN PRESS

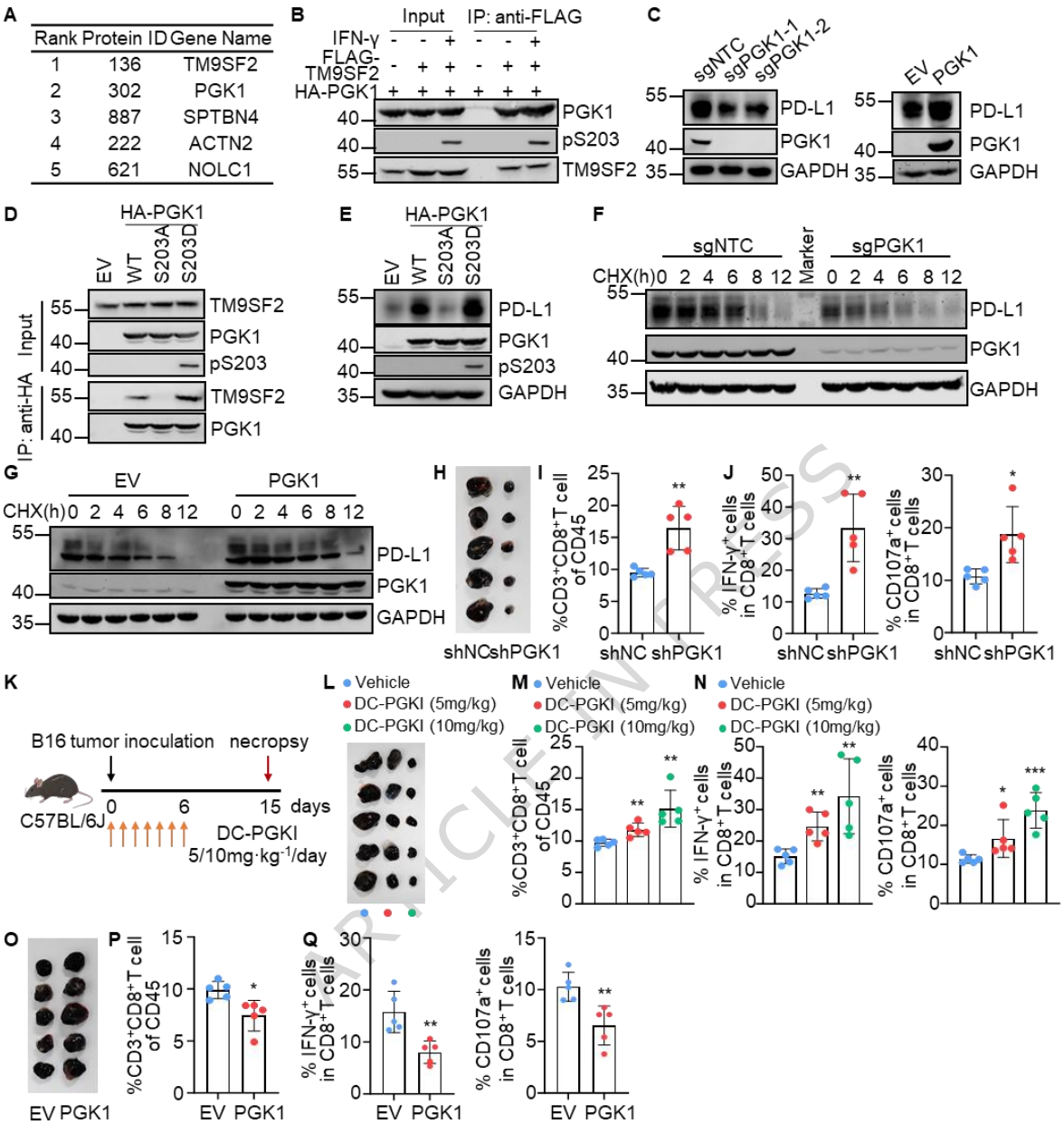

Fig. 3. TM9SF2 interacts with PGK1 to suppress CD8⁺ T cell function.

(A) Top five identified positive regulators ranked by enrichment scores from the immunoaffinity purification-mass spectrometry (IP-MS) screen. Immunoprecipitation was performed using anti-FLAG beads in HEK293T cells transfected using TM9SF2-FLAG.

For **B-E** and **G**, HA antibody is used for the detection of HA-tagged PGK1.

(B) Co-immunoprecipitation assays validating the interactions between TM9SF2 and PGK1 in H460 cells after 48 hours of IFN-γ stimulation (100 ng/mL).

(C) Western blot analysis of PGK1 and PD-L1 in H460 cells transduced with PGK1 sgRNAs versus sgNTC or H460 cells overexpressing HA-tagged PGK1 (n = 3 independent experiments).

(D) Co-immunoprecipitation assays demonstrating the association between TM9SF2 and PGK1 wild-type, S203D (phosphorylation-mimetic mutant), or S203A (phosphorylation-deficient mutant).

(E) Western blot analysis of PD-L1 levels in PGK1-depleted H460 cells transfected with PGK1 wild type or phospho-mutants.

ARTICLE IN PRESS

(F-G) The half-life of PD-L1 was assessed in H460 cells with PGK1 depletion or overexpression following treatment with CHX (25 μg/mL).
For **H-J**, C57BL/6J mice underwent subcutaneous injection with B16 cells transduced with PGK1 shRNA or control shRNA.
(H) Representative images and volumes of B16 tumors.
(I) Proportions of tumor-permeating $CD8^+$ T cells in tumors (n = 5 mice).
(J) Flow cytometry analysis of IFN-γ and CD107a levels in tumor-permeating $CD8^+$ T cells in tumors (n = 5 mice).
(K) Schematic of the experimental design: For **L-N**, C57BL/6J mice were subcutaneously inoculated with B16 cells followed by daily intraperitoneal administration of DC-PGKI (a PGK1 inhibitor, 5 and 10 mg/kg) for one week.
(L) Representative image of B16 tumors.
(M) Proportions of tumor-permeating $CD8^+$ T cells in tumors (n = 5 mice).
(N) The proportions of IFN-γ^+ and $CD107a^+$ tumor-permeating $CD8^+$ T cells in tumors (n = 5 mice).
For **O-Q**, C57BL/6J mice were injected with B16 cells overexpressing PGK1 or EV.
(O) Representative image of B16 tumors.
(P) Proportions of tumor-permeating $CD8^+$ T cells in tumors (n = 5 mice).
(Q) Flow cytometry analysis of IFN-γ and CD107a levels in tumor-permeating $CD8^+$ T cells in tumors (n = 5 mice).
Data are presented as mean ± SD. *p < 0.05; **p < 0.01; ***p < 0.001; ****p < 0.0001. Source data are provided as a Source Data file.

ARTICLE IN PRESS

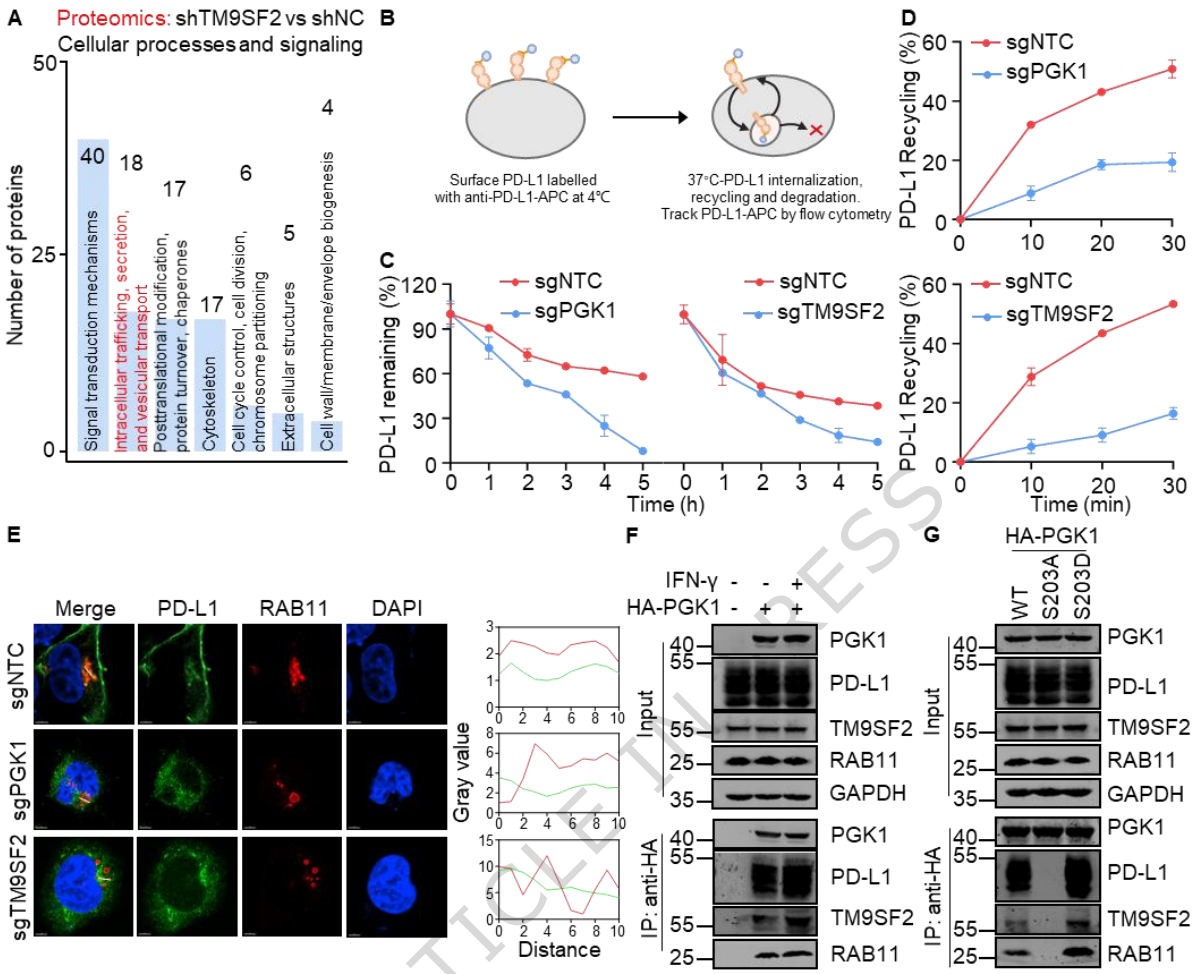

Fig. 4. TM9SF2-PGK1 maintains PD-L1 expression by facilitating endosomal recycling.

(A) Bar plot showing altered cellular processes and signaling pathways in shTM9SF2 H460 cells compared to shNC cells.

(B) A schematic of the PD-L1 surface internalization assay in H460 cells transduced with sgRNAs is shown.

(C) Surface PD-L1 retention in H460 cells was measured by flow cytometry after genetic depletion of PGK1 or TM9SF2 (*n* = 3 independent experiments).

(D) PD-L1 recycling was quantified by flow cytometry in H460 cells following PGK1 or TM9SF2 knockout (*n* = 3 independent experiments).

(E) Immunofluorescence showing PD-L1 colocalization with RAB11 in sgPGK1 or sgTM9SF2 H460 cells versus sgNTC (PD-L1 in green, RAB11 in red, DAPI in blue). Scale bar: 5 μm. The right panels display intensity profiles of PD-L1 versus RAB11 following the white line.

For **F-G**, HA antibody is used for the detection of HA-tagged PGK1.

(F) Co-immunoprecipitation assay demonstrating TM9SF2 interaction with PGK1, RAB11, and PD-L1 in H460 cells, with or without IFN-γ treatment (100 ng/mL, 48 hours).

(G) Co-immunoprecipitation assay evaluating interactions of PGK1 wild-type and its phospho-mutants (S203A and S203D) using TM9SF2, PD-L1, and RAB11 in H460 cells.

Data are presented as mean ± SD. *p < 0.05; **p < 0.01; ***p < 0.001; ****p < 0.0001. Source data are provided as a Source Data file.

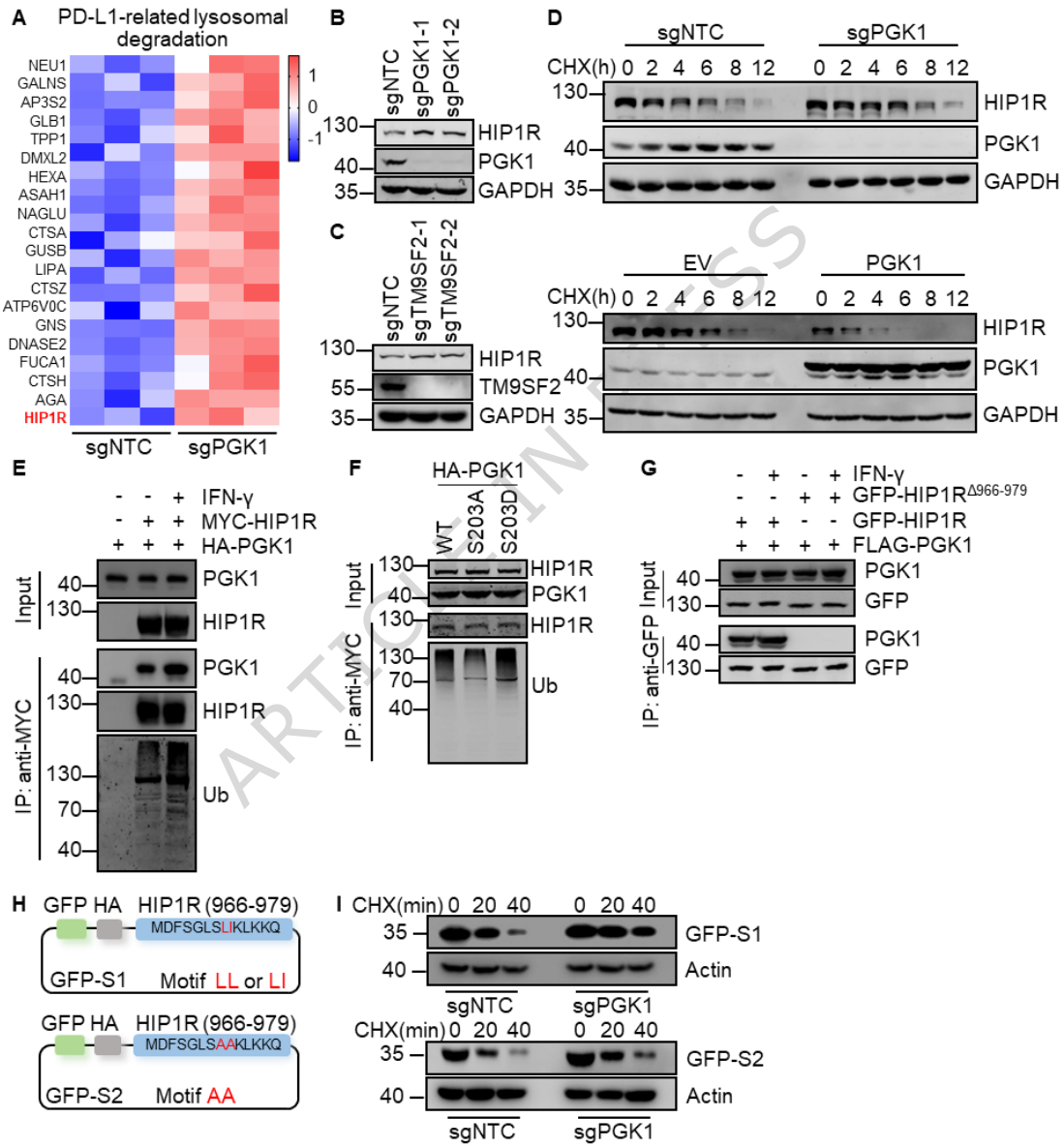

Fig. 5. TM9SF2-PGK1 complex hinders lysosomal sorting by degrading the PD-L1 lysosomal carrier HIP1R.

(A) Heatmap showing increased proteins involved in PD-L1 lysosomal degradation in sgPGK1 H460 cells versus sgNTC cells.

(B-C) Western blot of HIP1R levels in sgPGK1 (B) and sgTM9SF2 (C) H460 cells versus sgNTC cells (*n* = 3 independent experiments).

ARTICLE IN PRESS

For **D-F**, HA antibody is used for the detection of HA-tagged PGK1.

(D) Half-life analysis of HIP1R abundance in CHX (25 μg/mL)-treated H460 cells with PGK1 depletion or HA-PGK1 overexpression.

(E) Western blot analyses of HIP1R ubiquitination in H460 cells reconstituted with MYC-HIP1R and HA-PGK1 for 36 hours, followed by treatment with MG132 (10 μM, 8 hours) and with or without IFN-γ administration (100 ng/mL, 8 hours). MYC antibody is used for the detection of MYC-tagged HIP1R.

(F) Western blot analyses of HIP1R ubiquitination in HEK293T cells reconstituted using MYC-HIP1R and HA-PGK1 wild-type and phospho-mutants for 36 hours, followed by MG132 treatment (10 μM, 8 hours).

(G) Co-immunoprecipitation analysis examining IFN-γ effects on PGK1 association with GFP-HIP1R$^{\Delta 966\text{-}979}$ and GFP-HIP1R. H460 cells transfected with FLAG-PGK1 and either GFP-HIP1R or GFP-HIP1R$^{\Delta 966\text{-}979}$ were treated with IFN-γ (100 ng/mL, 8 hours). Flag antibody is used for the detection of FLAG-tagged PGK1 and GFP antibody is used for the detection of GFP-tagged HIP1R.

(H) A schematic of GFP fusion constructs is shown, including HIP1R lysosomal sorting signal (LL/LI, GFP-S1) and its corresponding mutant (AA, GFP-S2).

(I) CHX-chase assay showing GFP-S1 and GFP-S2 protein levels over time in sgPGK1 or sgNTC H460 cells treated with CHX (25 μg/mL).

Source data are provided as a Source Data file.

ARTICLE IN PRESS

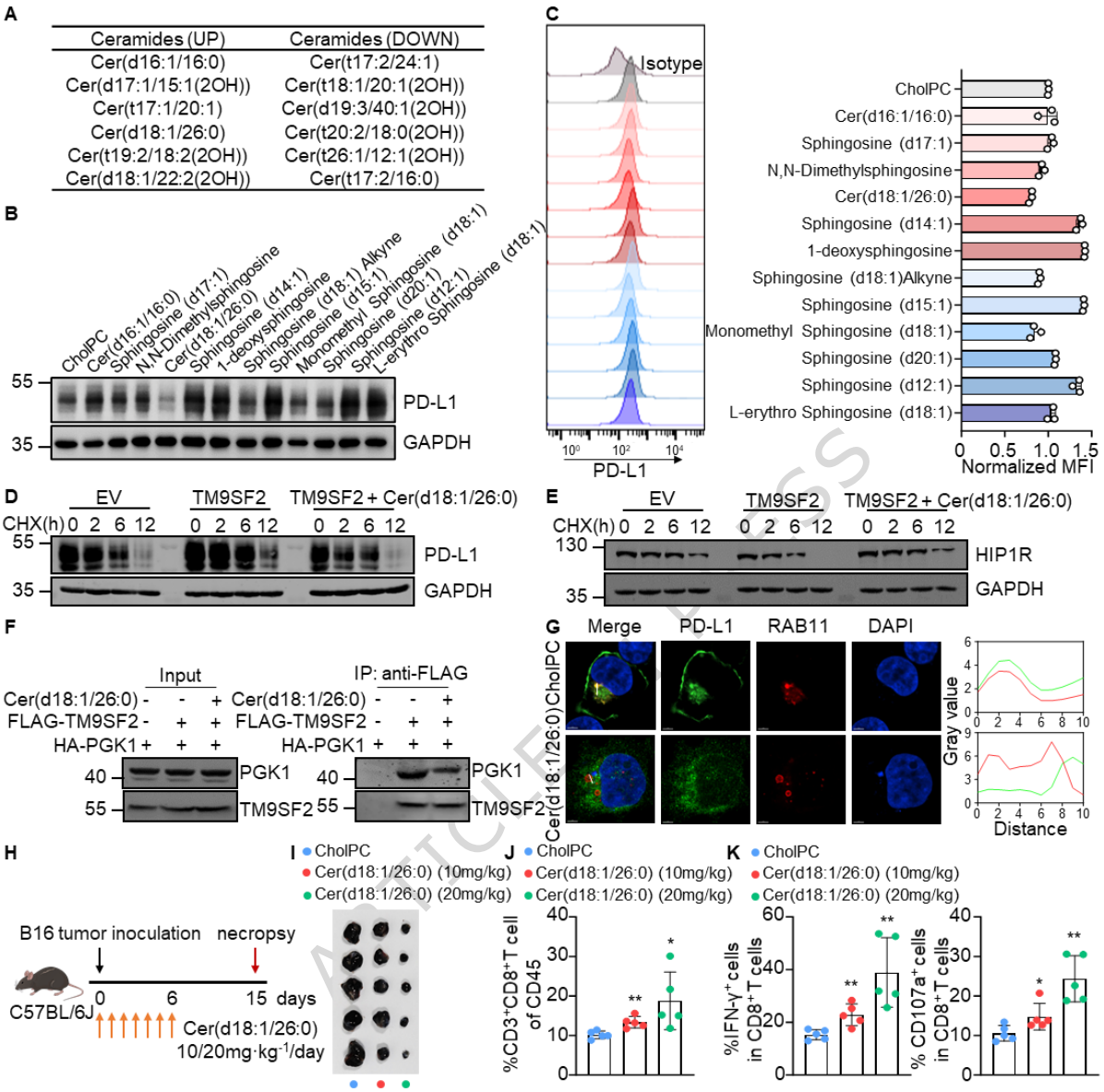

Fig. 6. Cer(d18:1/26:0) dissociates the TM9SF2-PGK1 Complex to suppress PD-L1 expression and promote anti-tumor immunity.

(A) Summary of ceramides that were up- or down-regulated following TM9SF2 depletion in H460 cells from lipidomics analysis.

(B) PD-L1 levels were analyzed using Western blot in H460 cells administered cholesteryl:phosphatidylcholine (CholPC) alone or CholPC loaded with ceramides and derivatives (31.25 μM, 40 hours).

(C) PD-L1 surface levels in H460 cells given cholPC alone or cholPC loaded with ceramides and derivatives (31.25 μM, 40 hours) (*n* = 3 independent experiments).

(D-E) Half-life analysis of PD-L1 or HIP1R concentrations in H460 cells overexpressing TM9SF2 for the indicated time points following CHX (25 μg/mL) treatment. Cells underwent pre-treated using 31.25 μM cholPC loaded with Cer(d18:1/26:0) for 40 hours.

(F) Co-immunoprecipitation analysis investigating the effect of Cer(d18:1/26:0) on the interaction between PGK1 and TM9SF2. HEK293T cells pre-transfected with HA-PGK1 or FLAG-TM9SF2 were

ARTICLE IN PRESS

treated with or without Cer(d18:1/26:0) (31.25 μM, 40 hours). HA antibody is used for the detection of HA-tagged PGK1.
(G) Immunofluorescence showing colocalization of PD-L1 with RAB11 in H460 cells with or without Cer(d18:1/26:0) treatment (31.25 μM, 40 hours). (PD-L1 in green, RAB11 in red, DAPI in blue.) Scale bars: 4 μm. Intensity of PD-L1 and RAB11 following the white line are shown in right panels.
(H) Schematic of the experimental protocol: For **I-K**, C57BL/6J mice were subcutaneously inoculated with B16 cells and then administered intraperitoneal injections of either CholPC or Cer(d18:1/26:0) (10 and 20 mg/kg/day) for one week. All statistical comparisons were performed against the CholPC-treated control group.
(I) Representative image of B16 tumors.
(J) Proportion of tumor-permeating $CD8^+$ T cells in B16 tumors (n = 5 mice).
(K) IFN-γ and CD107a levels in tumor-permeating $CD8^+$ T cells in B16 tumors (n = 5 mice).
Data are presented as mean ± SD. *p < 0.05; **p < 0.01; ***p < 0.001; ****p < 0.0001. Source data are provided as a Source Data file.

ARTICLE IN PRESS

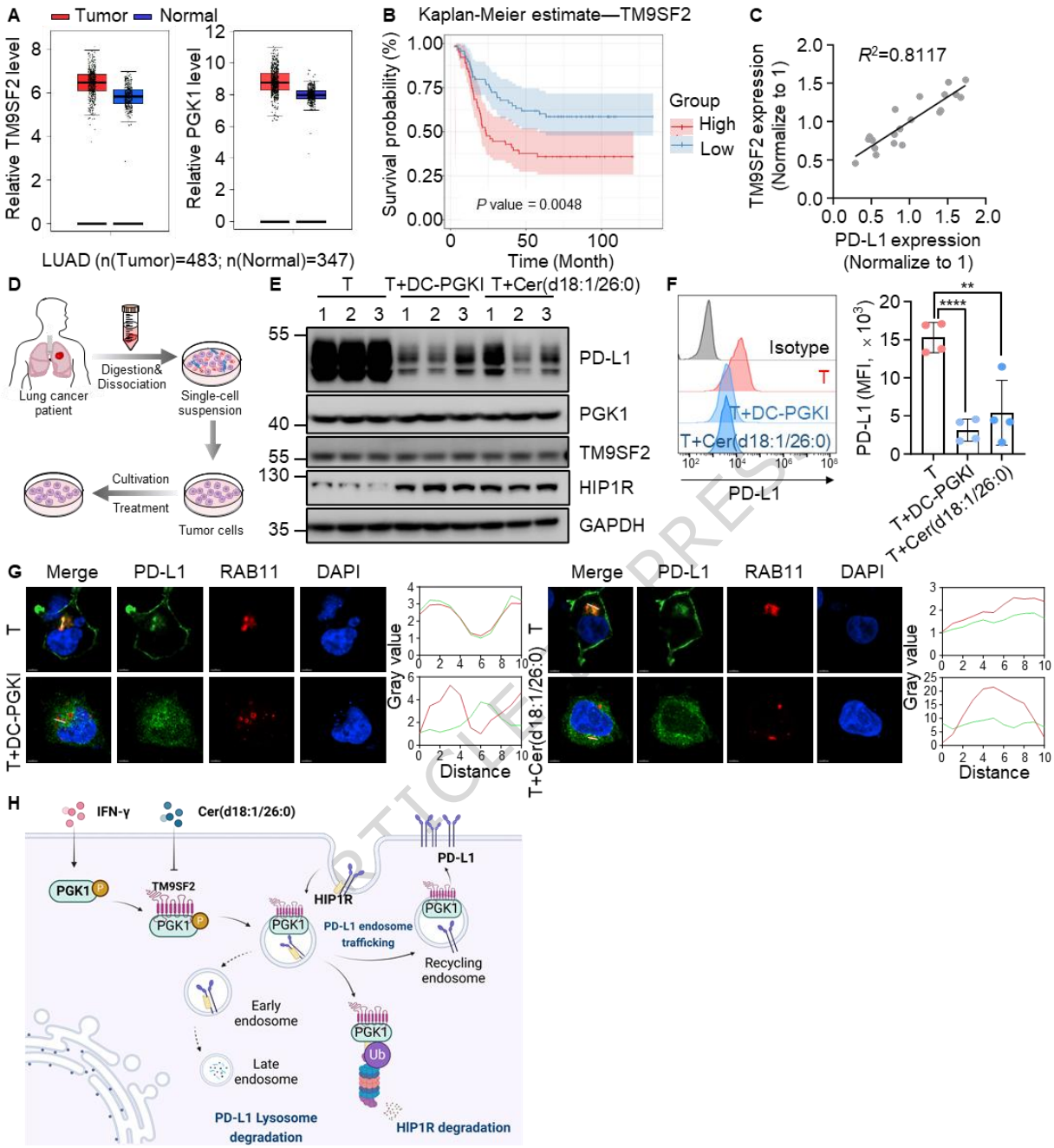

Fig. 7. Therapeutic potential for targeting TM9SF2-PGK1 complex in human lung cancer.

(A) TM9SF2 and PGK1 gene signature expression in LUAD; Pancreatic tumor tissue (Tumor, red) and Normal pancreatic tissue (Normal, blue) based on TCGA data analyzed via GEPIA2. (*n* (Tumor) = 483, *n* (Normal) = 347; *n*: number of patients). The box extends from the first to the third quartile (Q1 to Q3), with a line at the median. The whiskers extend to the most extreme data points within 1.5 times the interquartile range (IQR) from the box edges, and any points beyond are considered outliers.

(B) Kaplan-Meier survival curves for AML patients possessing high (red) or low (blue) TM9SF2 levels in the TARGET-AML cohort, analyzed using R software (version 4.1.0).

(C) Correlations between TM9SF2 and PD-L1 protein levels in human LUAD samples were evaluated using a Spearman correlation coefficient (R^2 value indicated, two-tailed).

ARTICLE IN PRESS

(D) Diagram outlining the experimental procedure for cancer cells isolated from patients with lung cancer and treated with DC-PGKI (10 μM, 24 hours) and Cer(d18:1/26:0) (31.25 μM, 40 hours).

(E) The expression of PD-L1, TM9SF2, PGK1, and HIP1R was analyzed via Western blot in cancer cells (T) treated with DC-PGKI and Cer(d18:1/26:0). Cancer cells were isolated from lung cancer patients.

(F) Representative histograms and bar plots of surface PD-L1 expression in cancer cells (T) treated with DC-PGKI and Cer(d18:1/26:0) (n = 4 independent experiments).

(G) Immunofluorescence showing co-localization of PD-L1 with RAB11 in human lung cancer cells treated with or without DC-PGKI or Cer(d18:1/26:0). (PD-L1 in green; RAB11 in red; DAPI in blue.) Scale bars: 4 μm. Intensity of PD-L1 and RAB11 following the white line are placed in right panels.

(H) Graphic abstract of the study. TM9SF2 facilitates PD-L1 plasma membrane recycling by recruiting PGK1 and suppressing the HIP1R-dependent lysosomal degradation pathway. Cer(d18:1/26:0) disrupts this complex, redirecting PD-L1 to lysosomal destruction and thereby boosting antitumor immune responses.

Data are presented as mean ± SD. *p < 0.05; **p < 0.01; ***p < 0.001; ****p < 0.0001. Source data are provided as a Source Data file. The Figure 7H was created in BioRender. Chen, S. (2026) (https://BioRender.com/o67s128).

ARTICLE IN PRESS